LAWRENCE
LIVERMORE
NATIONAL
LABORATORY

LLNL-JRNL-701400

# Modelling of ELMs and ELM control

G. T. A. Huijsmans, C. S. Chang, N. Ferraro, L. Sugiyama, F. Waelbroeck, X. Q. Xu, A. Loarte, S. Futatani

August 25, 2016

Physics of Plasmas

**Disclaimer**

This document was prepared as an account of work sponsored by an agency of the United States government. Neither the United States government nor Lawrence Livermore National Security, LLC, nor any of their employees makes any warranty, expressed or implied, or assumes any legal liability or responsibility for the accuracy, completeness, or usefulness of any information, apparatus, product, or process disclosed, or represents that its use would not infringe privately owned rights. Reference herein to any specific commercial product, process, or service by trade name, trademark, manufacturer, or otherwise does not necessarily constitute or imply its endorsement, recommendation, or favoring by the United States government or Lawrence Livermore National Security, LLC. The views and opinions of authors expressed herein do not necessarily state or reflect those of the United States government or Lawrence Livermore National Security, LLC, and shall not be used for advertising or product endorsement purposes.

**LLNL-JRNL-701400**

# Modelling of ELMs and ELM control

G.T.A. Huijsmans[1], C.S. Chang[2], N. Ferraro[3], L. Sugiyama[4], F. Waelbroeck[5], X.Q. Xu[6] , A. Loarte[1], S. Futatani[7]

[1]ITER Organization, Route de Vinon sur Verdon, 13115 Saint Paul Lez Durance, France
[2]Princeton Plasma Physics Laboratory, Princeton University, Princeton, New Jersey 08543, USA
[3]General Atomics, P.O. Box 85608, San Diego, California 92186-5608, USA
[4]Laboratory for Nuclear Science, Massachusetts Institute of Technology, Cambridge, Massachusetts 02139-4307, USA
[5]Institute for Fusion Studies, University of Texas at Austin, Austin, Texas 78712, USA
[6]Lawrence Livermore National Laboratory, Livermore, California 94551, USA
[7]Ecole Centrale de Lyon, 69130 Écully, Lyon, France

## Introduction

The ITER scenario to obtain an energy amplification Q = 10 is based on the well-established ELMy H-mode. In this scenario about 20-40% of the energy losses across the plasma boundary are due to Edge Localised Modes (ELMs). ELMs have been identified as MHD instabilities destabilised by the large pressure gradients and the associated bootstrap current in the H-mode pedestal. Each ELM can expel a significant fraction of the plasma energy and density on a typical time scale of a few hundred microseconds. Extrapolating the ELM energy loss from current experiments to ITER, based on the observed scaling with collisionality [Loarte2003], leads to the prediction of very large losses per ELM of up to 10% of the plasma thermal energy. The time scale for the energy flux to the divertor has been found to scale well with the parallel propagation time, $\tau_{//}$~$L/c_s$, where L is the connection length, $c_s$ the sound speed. This time scale is expected to be in the range of 250-500 μs, similar to the time scale in current machines. As a consequence of the large thermal energy content of ITER plasmas, the large fraction of the energy lost per ELM and the time scales, the expected energy flux to the divertor will be significantly larger in ITER compared to present experiments. Natural ELMs in ITER are likely to lead to enhanced erosion of the divertor. In order to avoid a reduction of the lifetime of the divertor, the amplitude of ELMs in ITER will need to be controlled to be below 0.7MJ per ELM [Loarte2013].

The control of ELMs can be achieved either by an increase in the ELM frequency or by a complete stabilisation of ELMs. The total ELM energy losses appear to be largely independent of the ELM frequency, an increase in the frequency leads to smaller losses per ELM and a reduction in the peak heat loads. An increase in ELM frequency can be achieved by providing an external trigger for the ELM, like for example, the injection of frozen hydrogenic pellets [Lang2004] or the application of fast variations ("kicks") vertical position of the plasma [Degeling2003]. A reduction of the ELM energy loss to 0.7MJ in ITER will require an increase of the ELM frequency by a factor of 30 over the natural ELM frequency. Complete stabilisation of ELMs has been obtained in DIII-D by applying an external magnetic field perturbation [Evans2004]. In other tokamaks, the application of external magnetic perturbations has been

seen to lead to an increase of the ELM frequency [Kirk20012,Suttrop2011,Jeon2012,Liang2007, Canik2010]. In ITER, there will be two systems for ELM control, a high frequency pellet injector system [Murayama2012] and a set of 27 magnetic field coils inside the vacuum vessel [Daly2012]. Vertical kicks may be an option for ELM control in ITER at plasma currents up to 10 MA but this method will not be available at the larger plasma currents needed for Q=10 operation [Loarte2013].

The expected energy loss per ELM in ITER is based on the extrapolation from current experiments of the scaling of the ELM size with collisionality. There is however no underlying physics model that would explain or justify the collisionality as the relevant parameter. In fact, a reduction of the ELM size with increasing density (relative to the Greenwald density $N_{GW}\left[10^{20}m^{-3}\right]=I\left[MA\right]/\pi a\left[m\right]^2$ ) has also been observed [Loarte2003] be it with a larger scatter in the data. ITER plasmas will be unique in the sense that ITER will operate at low collisionality and high relative density $N/N_{GW}$ at the same time. This regime cannot be obtained in current experiments. The same issue arises in the extrapolation of the results of ELM stabilisation with RMP coils from current experiments to ITER. In DIII-D ELM stabilisation has been obtained at low collisionality [Evans2008] whereas in AUG the stabilisation of type-I ELMs requires a minimum density above a given fraction of the Greenwald density [Fischer2012] (DIII-D also achieved ELM stabilisation at high collisionality [Evans2004]). It is therefore important to develop physics models and a predictive simulation capability of the complete ELM cycle in order to improve the confidence of the predictions of ELMs and ELM control methods in ITER.

In this paper, we describe the modelling of ELMs (section 2) and ELM control methods in ITER: externally applied magnetic perturbations (section 3) and pellets (section 4). The aim of this paper is not a complete review on the subject of ELM and ELM control modelling but rather to describe the current status and discuss open issues.

Alternative methods for ELM control not further discussed here are the trigger of ELMs by fast “kicks” of the vertical position of the plasma, the application of ECRH (AUG,TCV), LHCD (EAST) and ELM free QH-mode and I-mode plasmas.

## MHD Simulations of ELMs

In its simplest model, the ELM cycle can be separated into 3 phases. In the first phase, as the H-mode pedestal build up, the plasma moves from an MHD stable state, crossing the ideal MHD stability limit, to an MHD unstable state, either through an increase of the H-mode pedestal pressure gradient [Saarelma2013] and/or through an increase of the width of the pedestal [Groebner2009,Scannel2013]. The relevant ideal MHD stability limits are nowadays well known and are due to the onset of ballooning modes driven by the edge pressure gradients, external kink (peeling) modes driven by the bootstrap current associated with the edge pressure gradient or the onset of so-called peeling-ballooning modes driven by both the edge pressure gradient and current [Huysmans2005]. The time scale for an MHD instability driven through the stability boundary can be estimated as $\tau \sim \tau_E^{1/3}\tau_A^{2/3}$ [Callen1999] where $\tau_E$ is a typical confinement time, $\tau_A$ is the Alfven time. For an ELM, the relevant confinement time is the rebuilding of the pedestal after the previous ELM, i.e. $\tau_E \sim \Delta W/P_{SOL} \sim 1/f_{ELM}$ , inversely proportional with the ELM frequency. This yields a typical time scale of several tens of microseconds. In the second

phase the most unstable MHD mode(s) grow exponentially until the instability causes significant energy transport through convection or conduction. In this ELM crash phase, the MHD driven transport reduces the pedestal pressure leading to a collapse of the pedestal in typically some 100s of microseconds. This removes the drive of the MHD instability and the pedestal recovers. One of the important open questions is what determines the final state after the ELM crash. It is not obvious that this should be close the marginally stable state. In the case of very large MHD induced transport, the MHD perturbation has not yet decayed to a low amplitude when the pedestal returns to a stable state and the pedestal pressure can decay well below the marginally stable state.

In this section, the linear MHD stability limits are briefly discussed, followed by the status of non-linear MHD simulations of ELMs.

### *Linear MHD Stability limits*

The ideal MHD stability limits of the H-mode edge pedestal are due to the onset of pressure driven ballooning modes, current driven kink (or peeling) modes or a combination of the two instabilities the so-called peeling-ballooning modes. The observed maximum pedestal pressure gradients before an ELM are in good agreement with ideal MHD stability calculations [Snyder2004, Saarelma2005, Burckhart2013].

As an illustration, figure 1 shows the ideal MHD stability limits [Maget2013] for an ITER Q=10 scenario as calculated with the MISHKA-1 code. The maximum stable pedestal pressure in this ITER scenario is between 100 and 130 kPa [Maget2013, Saarelma2012], for a “given” pedestal width of 5.4cm. The limit is consistent with the confinement requirements to obtain Q=10. The maximum pedestal pressure does depend on the assumed pedestal width. The accessibility of the pedestal MHD limits is not often discussed. However as shown in [Maget2013], for this particular ITER scenario, the kink limit is not accessible due to the saturation of the increase of the bootstrap current with decreasing density. However, the limit due to the external kink mode is sensitive to the assumed current at the separatrix.

The EPED model [Snyder2011] combines the pedestal ideal MHD stability limits with a local pressure gradient limit due to kinetic ballooning modes to give a prediction for both the height and width of the pedestal. The kinetic ballooning mode limit is approximated by the infinite-n ideal MHD ballooning limit [Groebner2013]. The EPED predictions for the pedestal height are in good agreement, within an error bar of 20%, with measured pedestal heights for a large number of discharges on multiple machines. For ITER, the EPED model predicts a pedestal pressure of 92kPa at a pedestal width of 0.04 in normalised poloidal flux [Snyder2011] with a strong dependence of the achievable pedestal pressure on the pedestal density [Snyder2012].

The relatively good agreement between the observed maximum pedestal pressure and the ideal MHD stability limits appears to indicate that the non-ideal MHD effects such as resistivity, diamagnetic flows, toroidal and poloidal flows do not have a large influence on the stability limits. The stabilising influence of the diamagnetic terms is commonly taken into account using a simple analytic expression, calibrated on a limited set of calculations self-consistently including diamagnetic terms. The effectiveness of the diamagnetic stabilisation is typically reduced by a factor of two compared to the analytic expression. This is likely due to the radial variation of the diamagnetic frequency calibration across the width of the pedestal (and the MHD instability) leading to a reduced or even incomplete stabilisation [Hastie2000,

Huysmans2001,Xu2010]. The ion diamagnetic stabilization on high-n modes disappears when the large density gradient is taken into account [Xi2013]. But gyro-fluid simulations show that the finite Larmor radius (FLR) effect can effectively stabilize high-n modes, so the ion diamagnetic effect alone is not sufficient to represent the FLR stabilizing effect. It has been demonstrated that additional gyroviscous terms must be kept in the two-fluid model to recover the linear results from the gyro-fluid model. Nonlinear simulations show that the density variation significantly weakens the E×B shearing at the top of the pedestal and thus leads to more energy loss during ELMs. As the diamagnetic terms scale with the toroidal mode number, the stabilisation is most efficient for high-n ballooning modes. The relative amplitude of diamagnetic stabilisation is smaller for larger machines as it scales with the inverse of the ion-cyclotron frequency normalised to the Alfven time. In ITER, with a high pedestal density, the diamagnetic stabilisation is expected to be small [Maget2013] for the most unstable medium-n peeling-ballooning modes.

The shear in the toroidal rotation profile in the pedestal is typically found to have a stabilising influence on the high-n ballooning modes [Snyder2007,Saarelma2007,Pankin2007]. The stabilisation can be attributed to the shearing of the ballooning mode structure. For medium-n modes, both stabilisation [Saarelma2007] and destabilisation have been observed [Snyder2007,Aiba2010]. The effect on the stability of peeling modes is negligible [Aiba2010].

In JT60U, analysis of the pedestal stability [Aiba2011] showed that the pedestal is well below the MHD stability limit when the (counter) toroidal rotation was neglected. In this case, the counter toroidal rotation was found to have a significant destabilising effect on the most unstable modes. Including the experimental rotation profile in the stability analysis shows the experimental point is in good agreement with the stability limit. In this case, the de-stabilising effect is not attributed to the Kelvin-Helmholtz drive but is related to the difference in the eigenmode frequency and the toroidal rotation frequency. In the analysis the rotation was included self-consistently in both the equilibrium and the linear stability. In addition to changing the linear growth rates, the rotation shear can also significantly alter, i.e. reduce, the width of the linear eigenmode. This may have consequences to the ELM affected area and the ELM amplitude.

The contribution of the Kelvin-Helmholtz drive of the perpendicular (ExB) rotation in the pedestal was studied by [Xi2012] using the BOUT++ code in circular plasmas. The KH term was found to be destabilising for medium to large n ballooning modes, slightly stabilising for low-n modes. However, the effect only becomes significant when the rotation shear exceeds a certain threshold. In simulations with the JOREK code [Pamela2011] in JET x-point plasmas, the localised ExB flow in the pedestal was found to have a strong stabilising influence for the medium to high-n modes.

The impact of the shaped plasma geometry with x-point has been studied using edge two-fluid code BOUT++. A set of reduced magnetohydrodynamics (MHD) equations is found to simulate the linear P–B mode in both snowflake plus and standard (STD) single-null divertor configurations. Analysis shows that the implementation of snowflake geometry changes the local magnetic shear in the pedestal region, which leads to different linear behaviours of the P–B mode in STD and SF divertor configuration [MaNF2014].

A recurring question is the influence of the x-point on the linear stability of the peeling and ballooning modes. Conventional linear stability analysis considers the plasma closely up to but not including the

separatrix and a vacuum region outside. In this case, the stability of peeling modes [Huysmans2005] and peeling-ballooning modes [Saarelma2012] can depend on the choice of the distance of the assumed plasma boundary and the separatrix. This restriction is due to the use of a straight field line coordinate system and the (artificial) separation into an ideal MHD plasma region and a vacuum region inside the vessel. A solution to this problem would be to avoid the separation into plasma and vacuum and to include plasma on the whole domain on both closed and open field lines as is now commonly used for non-linear ELM simulations (see next section). A significant step forward from the modelling point of view would be to combine the whole domain approach with an extended two fluid MHD model including toroidal, poloidal and diamagnetic flows and parallel heat conduction. The flows would need to be included self-consistently in both the equilibrium and the linear stability. However, validation of the additional physics beyond the simple but robust ideal MHD model will be challenging. The dominant physics of the most unstable modes is well described by the ideal MHD model with the additional physics given only first order corrections to the marginal stability boundaries. Validation will require very accurate measurements of all the relevant profiles in the H-mode pedestal.

### *Non-linear MHD simulations of ELMs*

The non-linear MHD simulation of the complete ELM cycle is probably one of the most challenging numerical problems in MHD in tokamaks. The difficulties in MHD simulations in tokamak plasmas are generally due to the large variation of time scales, the low resistivity (high Lundquist numbers) and the large anisotropy in the parallel to perpendicular heat conduction. For ELM simulations, the time scales vary from the Alfven time scale of the MHD instabilities ($\tau_A$~μs) to the ELM repetition rate ($f_{ELM}$ ~ few Hertz for uncontrolled ELMs in ITER). A typical Lundquist number at the top of the pedestal in ITER is $S \sim 5 \times 10^9$, leading to very small scale structures and very high spatial accuracy requirements. The anisotropy of the parallel to perpendicular conduction at the ITER pedestal is $\kappa_{//}/\kappa_{\perp} \sim 10^{10}$ (for Braginskii, not flux limited parallel conduction). This leads to the need of very accurate numerical schemes to avoid artificial perpendicular diffusion. In addition to these complication common to many MHD applications, the simulations of ELMs has also more specific challenges. As ELMs occur at the edge of the plasmas with an x-point geometry, the simulation domain will need to include both the closed and open field lines. This includes the separatrix where at the x-point the local poloidal wave vector becomes very large. Simulating the ELM energy losses to the divertor and the first wall requires specific boundary conditions for the parallel velocity and the energy fluxes, as commonly applied in divertor physics codes). An additional complication is the medium to high-n toroidal mode number ($n \approx 6$-$20$) of the linearly most unstable (peeling-) ballooning modes with typically a range of unstable modes with comparable growth rates. At the edge the inverse aspect ratio is highest, increasing the toroidal mode coupling.

Due to these challenges in the simulation of ELMs, there are currently no published simulations of the full ELM cycle, i.e. evolving the plasma from a stable inter-ELM state, through the instability back to a stable state. Multiple ELMs have been simulated in circular geometry and a reduced two-fluid MHD model [Thyagaraja2010]. High frequency ELMs have been obtained in flux tube geometry using a reduced Braginskii model in the resistive ballooning mode limit [Kleva2007], more likely to be relevant for type-III ELMS.

A number of non-linear MHD codes, M3D [Park1999,Sugiyama2000], BOUT++ [Dudson2009], JOREK [Czarny2008], NIMROD[Pankin2007]) now have the capability to simulate ELMs in the shaped plasma

geometry with x-point approaching the experimentally relevant values for the resistivity and parallel heat conduction. At this stage in the developing simulation capability of ELMs, a common approach is to start the simulations from an unstable equilibrium. This avoids the slowly evolving phase passing from the stable to the unstable state. This approach is suitable for studying the physics of the non-linear evolution of the ELM and the energy and particle loss mechanisms. However, it is not possible to obtain a realistic evaluation of the ELM size with this approach as it is not clear by how much the plasma can exceed the stability limit before an instability grows to an significant size to prevent a further increase of the pedestal (gradients).

An example of a simulated ELM crash in a DIII-D discharge (#126006,t=3500ms) with the M3D code [ Sugiyama2012] is shown in Fig.2. The time scale of the initial outward ballooning burst over 100-200μs for this DIII-D case is consistent with experimentally observed crashes. After the initial ballooning outburst, the later ELM can proceed in a series of somewhat random oscillations, as a series of smaller edge disturbances grow and decay within a gradual overall damping.

The formation of filaments during the ELM crash is a characteristic feature present in many ELM simulations performed with the different MHD codes. These filaments are formed by the interchange motion of the ballooning mode instability which forms convective cells across the pedestal onto the open field lines. The convective cells, localised on the outboard side of the plasma, exchange high from the pedestal and low density from the scrape-off layer to form high density field-aligned filaments outside the separatrix and, in some cases, low density holes inside the plasma. The result strongly resembles the ballooning “filaments” observed experimentally. Also the typical radial speed of the order of km/s is in reasonable agreement between simulations [Huysmans2009, Holzl2012, Pamela2011, Pamela2013] and experimental observations.

The non-linear interaction due to the Maxwell stress leads to a strong growth of an n=0 poloidal flow in the vicinity of the pedestal [Huysmans2007,Sugiyama2012,Xia2013]. The n=0 flow shears off from the filaments from the main plasma. After this the ELM perturbation decays until a new burst of filaments grow and detach from the plasma. It seems likely that this poloidal flow leads to a saturation of the maximum amplitude of each of these bursts. More unstable plasmas lead to a larger number of bursts.

Strong toroidal mode coupling can lead to a significant difference between the behavior of ELMs that evolve from the interaction of multiple toroidal harmonics compared to those started from a single dominant harmonic. Because ballooning and peeling modes tend to have a range of harmonics with similar large growth rates, the first case appears to be more realistic. Large scale numerical simulations with the M3D extended MHD initial value code have explored [Sugiyama2009,2010,2012] this effect. They show that nonlinear toroidal interactions may provide a purely MHD explanation for the moderate observed ELM values $n$=10-15, even in cases where the linear unstable MHD modes are ballooning-like and have peak growth rates at much higher harmonics $n \geq 30$ [Sugiyama2010,2012]. Started with a full spectrum of toroidal harmonics at similar small amplitude, the MHD perturbation first grows at the highest harmonics allowed in the simulation, with the largest amplitude around the outer midplane similar to ballooning or peeling eigenmodes, but by the time it noticeably perturbed the total plasma edge density and temperature, the peak harmonics has decreased. Simultaneously, the amplitude in the outboard region closer to the top and bottom of the plasma, $\theta \sim \pm 60°$, grew comparable to that at the midplane, as shown in Fig. 2. This behavior was observed for $n_{max}$=23 and 47; in both cases the main ELM crash developed similar moderate harmonic numbers. The maximum nonlinear growth rate, which occurred shortly before the ballooning plasma fingers reached their maximum radial extent, was significantly smaller than the

linear growth rates, including at the same *n*. Two-fluid terms from the drift ordering had little effect nonlinearly.

The non-linear toroidal coupling can also lead to a toroidal and poloidal localisation of the filaments due to the beating of several linearly unstable toroidal modes [Krebs2013] leading to the growth of a highly localized helical band with a strong $n$=1 component with a few filaments instead of a full set of n toroidally equally distributed filaments. This effect is especially strong for spherical tokamaks at very low aspect ratio [Sugiyama2012] but has also been found in ELM simulations in AUG [Holzl2013]. It should be noted that in other cases, with a dominant single unstable toroidal harmonic, this coupling is not observed [Pamela2013]. Figure 3 illustrates some of the different filament structures obtained in ELM simulations in DIII-D, NSTX-like and AUG discharges. The resulting structures strongly resemble the ballooning "filaments" observed experimentally in both types of experiment. Both tokamaks and STs (e.g., DIII-D, TCV and NSTX) naturally tend to develop $n$=3 and $n$=1 components.

A second characteristic feature of non-linear MHD simulations of ELMs is related to the magnetic perturbation of the ballooning mode instability. The formation of a stochastic region during the ELM was found already in early non-linear ELM simulations [Huysmans2007]. In more recent simulations, the magnetic structures in the stochastic region was identified as being related to so-called magnetic tangles [Sugiyama2010,2012]. The presence of a magnetic X-point on the plasma boundary surface strongly influences the nonlinear character of edge modes, especially the large ELMs that have the most global character. In the equilibrium, magnetic field lines on the separatrix become increasingly toroidal as they approach the vicinity of the X-point and their intersection points on a given vertical plane become more closely spaced; at the X-point the field line is strictly toroidal. Mathematically, toroidal magnetic fields can be described as Hamiltonian systems with one (axisymmetric field) or two (non-axisymmetric [Boozer83]) degrees of freedom. An X-point in axisymmetric toroidal plasma corresponds to a hyperbolic saddle point. A local perturbation analysis [Lichtenberg92] shows that almost any small transverse perturbation of the separatrix surface (including ballooning and peeling modes in a plasma) produces field line splitting, where two limits for the perturbed field surface coexist near the X-point, one lying on the original equilibrium surface and the other forming transverse loops around it, that become narrower but longer as the field line approaches the X-point. The X-point is a fixed point. The resulting configuration is called a homoclinic tangle (for a single X-point) and the many intersections of the transverse field loops lead to a stochastic magnetic region around the plasma edge. In the 3D torus, the loops helical corrugations are aligned along the equilibrium field. Magnetic tangle structures have been extensively studied for applied RMP fields, based on the vacuum field generated by the external coils [Roeder2003,Evans2004]. Nonlinear simulations have shown show that ballooning modes can self-consistently generate a tangle-like perturbation [Sugiyama2009,2010]. The tangle feeds back on the nonlinear ELM evolution and contributes to the coupling of the unstable ballooning-type instability on the outboard side to the torus to the initially stable inboard side. Similar effects occur around an X-point outside, but near the plasma boundary.

A homoclinic tangle is limited to the separatrix surface and the interior region. Open field lines outside the separatrix may shift slightly in response, but do not split. The nonlinear simulations show that the field lines can extend well beyond the original plasma edge, especially very close to the X-point legs, as expected for a tangle. Where the extended tangles intersect the divertor, secondary strike points are formed leading to multiple stripes in the power deposition profile during the ELM. Figure 4 shows a

Poincare plot of the magnetic field structure during an ELM simulation in an ITER Q=10 scenario [Huijsmans2013].

With the formation of filaments and magnetic tangles one can identity different loss mechanisms for the thermal energy during the ELM. The ejection of filaments, due to the convective motion of a ballooning mode corresponds to convective energy losses of density and energy. The losses from the filaments, losses once outside plasma, are both in parallel direction along the filament and due to the radial movement of the filament into the first wall. The magnetic tangles and the stochasticity cause a direct connection of field lines from inside the plasma to the divertor (or the first wall). This leads to large parallel conductive losses causing mostly a reduction in the pedestal temperature. The relative importance of these two loss channels may account for the experimental classification of ELMs into so-called convective and conductive ELMs [Leonard2002]. Convective ELMs, characterised by significant density losses and small temperature changes, are small amplitude ELMs at high density where the parallel conduction is low. Conductive ELMs, with large energy losses and density losses comparable to the convective ELMs, occur at low density. The minimum ELM density loss (for both convective and conductive ELMs) would then be determined by the ejected filaments. If the conducted losses are indeed related to the magnetic tangles, one would expect a correlation with the amplitude (and duration) of the magnetic perturbation of the ELM. This remains to be verified experimentally.

**MHD models**

The BOUT++ code has been applied to investigate the influence of different MHD models from 3-field model, which evolves vorticity, pressure and vector potential [Xu2010,2011,Dudson2011,Xi2012] to 6-field [Xia2012,2013,2013a,Xu2013] and gyro-Landau-fluid models [Xu2013] on the linear stability of the pedestal and the ELM crash. Through these comparisons, we can see that although the equations of the six-field model are much different from the original three-field model, both linear and nonlinear activities of peeling-ballooning instability are still close. This result indicates that the peeling-ballooning instability, ion diamagnetic effects, resistivity and hyper-resistivity, which can be well described by the three-field model, are the dominant physics effects during the burst of ELMs. So the three-field model is good enough to simulate peeling-ballooning instabilities and early nonlinear phase of ELM crashes if the simulations start from a strong unstable equilibrium. However, additional physics is important from 6-field and gyro-Landau-fluid models if the simulations start from an equilibrium close the marginally stable state [Xia2013a,XiPoP2014]. Furthermore, ELM dynamics is a multi-scale problem, ranging from meso-scale MHD events to micro-scale turbulent dissipation due to electron gyro-radius effects. In order to simulate a ELM cycle and perform experimental validations, sophisticated multi-field models are necessary to obtain (1) ELM power loss via separate ion and electron channels; (2) ELM power depositions on plasma facing components (PFCs); and (3) self-consistent turbulence and transport between ELMs for the pedestal profiles rebuild.

**Power deposition**

- The cause for concern with respect to ELMs in ITER is due to the predicted large ELM heat fluxes to the divertor. The peak heat flux is determined by the total ELM energy loss, the time scale of the losses and the “wetted” area, the area over which the energy is distributed. Experimentally, the wetted area is seen to increase linearly with the amount of energy lost at each ELM [Eich2011]. ELM simulations in JET-like geometry with the JOREK code [Huijsmans2013] show that the origin of this broadening of the wetted area

is due to the correlation between the ELM size and the amplitude of the magnetic perturbation (of the ballooning mode). The larger magnetic perturbation leads to more pronounced magnetic tangles and more secondary strike points at the divertor, distributing the energy over a larger area. Also the filaments ejected from the plasma contribute to the widening of the wetted area. Simulations in MAST [Pamela2013] and ITER [Huijsmans2013] show, in the case of convective ELMs with a small magnetic perturbation, a significant broadening caused by the energy in the filaments convected along the unperturbed magnetic field. Both mechanisms lead to a spiral pattern of the heat flux on the divertor [Huysmans2009, Pamela2011]. The MHD simulations typically find that the ELM driven heat flux goes predominantly to the outer divertor, due to the ballooning character of the MHD instability. This also leads to a time delay for the power to arrive at the inner divertor, due to the longer connection length to the outboard. Experimentally, the ELM losses are larger on the inner divertor, opposite to the simulation results. This is one of the open problems remaining to be addressed. **Particle fluxes from BOUT++ show features consistent with measurements on upper and lower divertor plates when the magnetic field is reversed on EAST[GuoPoP2014].**

**Validation**

Even though the ELM simulations are still in a relatively early stage of development, the validation of the simulation results against experimental observations can already be very useful. Validation is essential to have any confidence in predictions made for ELMs in ITER. Validation can take the form of comparing global trends such as the observed scaling of the amplitude of the ELM energy losses with collisionality, the scaling of the ELM duration with the parallel ion sound speed, the change in the relative density and energy losses as a function of the pedestal density, the scaling of the width of the ELM power footprint with the ELM amplitude. In [Pamela2011], the relative ELM energy losses in ELM simulations in JET were found to increase with decreasing collisionality whereas no dependence was found for the relative density losses. This trend is similar to the one observed in experiments [Leonard2002,Leonard2006], although not as strong. This points to the importance of the parallel heat conduction for the energy losses with a strong temperature dependence and the role of filaments as the source of density losses, independent of collisionality. However, it should be noted that the ELM amplitudes are determined from an unstable starting equilibrium, not yet from a full ELM cycle. This may have an influence on the results.

A more direct validation can be obtained through the comparison of fast diagnostic measurements of the ELM precursors, ELM crash, ELM affected area and the power and particles fluxes to the divertor. Fast visible light cameras give detailed information on the structure and evolution of the filaments ejected by the ELM, such as on EAST shown in Fig.8 [HahmNF2013]. Figure 5 show an example of a direct comparison of a camera image of an ELM in MAST with the predicted image of the $D_\alpha$ light based on the temperature and density in the filaments from the simulation of an ELM with the JOREK code [Pamela2013]. The radial width of the filaments as they detach from the plasma can be measured with fast Thomson scattering of the density profile. Comparison with simulations shows good agreement, including the fact that the filament structure is much less visible in the electron temperature. The same simulations also show good agreement in the footprint of the energy and particle fluxes as observed with the visible and IR cameras in MAST [Pamela2013]. The recent development of ECE imaging diagnostics [Boom2011, Yun2011, Park2012] give very detailed 2D data of the ELM fluctuations. This will be very

valuable for detailed validation of the ELM dynamics. First comparisons of ECE imaging data with BOUT++ linear mode structures show good agreement [Park2012, KimNF2014]. Direct comparison with fast magnetics data may be more challenging as the magnetic response may depend on the interaction with a conducting wall. Magnetics data can give information on the toroidal localisation of the ELM perturbation [Wenninger2012]. Similar strong localisation is also found in ELM simulations in AUG using the JOREK code (see Fig3c) [Hoelz2012].

**Discussion**

One of the important questions for extrapolation to ITER is what determines the amplitude of the ELM energy losses. Assuming that one cannot significantly cross an ideal MHD stability boundary, the ELM losses are determined by the state to which the pedestal relaxes during the ELM. Thus, the question is: what determines this state immediately after an ELM. However, there has been little emphasis in recent studies both experimentally and from simulations. A return to the marginally stable state would lead to too small ELMs. This may be enhanced when the ELM itself changes the marginal stability boundary. It has been proposed in [Saarelma2007], that the reduction in the plasma rotation due to an ELM may lower the marginal stability limit from the rotation stabilised higher limit to the zero rotation lower limit. This could be especially relevant in spherical tokamaks with a large rotation. The locking of the rotation or the reduction in rotation shear may also decrease the efficiency of the stabilisation of the turbulence in the H-mode pedestal, leading to an increased turbulent transport. The formation of magnetic tangles due to the magnetic perturbation of the ballooning mode leads to a direct connection from inside the original separatrix to the divertor. The resulting ELM energy losses depend on the parallel conduction and the lifetime of the tangles. The formation of an avalanche-like process may also contribute to increased energy losses. In this case, the flattening of the pressure in the pedestal leads to large gradients further inwards, destabilising additional MHD instabilities increasing the flattened region and moving the large gradients further inwards. This behaviour is sometimes observed in simulations, leading to very large ELM affected areas. However, this is mostly observed in case of high resistivity, raising the question whether this is relevant also for realistic values of the resistivity.

For more realistic simulation of ELMs, it is likely to be necessary to include more divertor physics in the non-linear MHD codes. This includes for example the divertor boundary conditions. In steady state the standard Bohm boundary conditions link the convective and conductive fluxes at the target through a constant sheath transmission factors, $\gamma_{SH}$. PIC simulations in 1D [Tskhakaya2009] show that during a transient ELM phase, $\gamma_{SH}$ can vary significantly in time. However, recent comparisons of 1D fluid simulations with PIC and Vlasov solutions indicate that the error in the parallel electron and ion heat fluxes at the divertor target due to the assumption of a constant $\gamma_{SH}$ in the fluid approach is relatively small [Havlickova2012]. In addition to the divertor boundary conditions, the divertor regime may also have a strong influence on the ELM driven heat loads. In the long term, predictions for ELMs in ITER will need to include a description of the high recycling, partially detached divertor.

As mentioned above, typical non-linear MHD ELM simulations start from an MHD unstable initial state and only consider a single ELM. This approach does not allow predictions for the amplitude of the ELM energy and particle losses, as these tend to depend on how unstable the initial state was (chosen to be). Simulations of a multiple full ELM cycles will be necessary such that the ELMs do not depend on the choice of the initial state. From simulations of multiple ELMs is in simplified geometry [Kleva2007, Thyagaraja2010] it appears that the diamagnetic terms in the MHD model are essential obtain a cycling

regime with repeated ELM crashes. A similar conclusion was reached from non-linear MHD simulations of sawteeth where in order to obtain repeated fast crashes requires a minimum threshold in the diamagnetic stabilisation [Halpern2011].

An alternative concept, based on the phase coherence time, was proposed in [Xi2014]. The interaction of many unstable peeling-ballooning modes destroy the phase coherence of the linear instability, giving not enough time to grow to large amplitude, leading to a background, peeling-ballooning, turbulence. The formation of discrete ELM like crashes requires a long enough “phase coherence time”, i.e. coherence between the pressure and potential (ExB flow) so that a mode can grow from the turbulence to large event. This concept leads to a non-linear criterion for the ELM onset.

## ELM Control methods: Resonant Magnetic Perturbations

The complete stabilisation of type-I ELMs with the application of external magnetic field perturbations was first observed in DIII-D at high collisionality [Evans2004] and at, ITER relevant, low collisionality [Burrell2005]. Type-I ELM stabilisation at high and medium collisionality was also observed in AUG [Suttrop2011] and KSTAR [Yeon2012] respectively. Experiments in MAST [Kirk2011] and JET [Lang2007], find mitigation of ELMs but no ELM stabilisation.

ITER will include a set of in-vessel ELM coils for the control of ELMs. The set of 27 coils is arranged in 9 coils sets in the toroidal direction with each coil set consisting of 3 coils, with 6 turns each. The coils are located above, below and in the mid-plane on the low field side vessel wall [Loarte2012, Daly2013]. At present, the requirements of the ITER coil currents are based on the criterion for the stabilisation as established in the DIII-D experiments [Fenstermacher2008]. This criterion sets the minimum amplitude of the applied magnetic perturbation in terms of a minimum width of the stochastic layer at the plasma boundary (Chirikov island overlap parameter > 1, in a region $\Delta\psi>0.165$). Applied to ITER, depending on the details of the plasma scenarios, this leads to a requirement on the coil current between $I_{RMP}$ = 20-75 kA-turns [Evans2013], This leaves some margin, for example for some RMP coil failures, with respect to the maximum coil current of 90 kA-turns.

The DIII-D ELM stabilisation criterion is not universal. In other machines, ELM mitigation, but not stabilisation, is observed while satisfying the criterion. One uncertainty in the predicted RMP current requirements comes from the response of the plasma to the applied external magnetic field perturbation. It is well known that a rotating plasma tends to shield the perturbations whereas in a static plasma the perturbations can penetrate [Fitzpatrick1998]. The shielding acts through the formation of radially localised current sheaths, located at (or close to) the rational q surfaces. These currents reduce the amplitude of the q=m/n harmonic at the rational surface. The amount of screening is influenced by the plasma rotation but also by the resistivity with increased shielding at low resistivity. The time scale for the build-up of the screening currents is inversely proportional to the resistivity [Becoulet2009]. In cylindrical geometry, the amplitude of the screened harmonic remains low inside the rational surface. In shaped plasmas in toroidal geometry, due to the coupling of poloidal harmonics, the mode amplitude as a function of radius typically has a minimum value at the rational surface.

For RMP ELM control, the dominant flow is due to the large ExB and diamagnetic flows in the H-mode pedestal. In particular, the screening and penetration of the external field is determined by the rotation of the electrons, as was found in kinetic [Heyn2008] and two-fluid MHD [Nardon2010, Becoulet2012] models. The initial cylindrical analysis was extended to more relevant toroidal plasmas with x-point geometry in [Ferraro2012, Orain2013]. The penetration is most effective for the m/n harmonic of the external perturbation whose rational surface is closest to the point (when it exists) where the electron fluid velocity has a zero. As a consequence, the m/n perturbation at the rational surface has a resonant window as a function of $q_{95}$ [Becoulet2012] in which the perturbation penetrates inwards. The width of this resonant window was found to depend on the amplitude of the externally applied perturbation.

The toroidal rotation will be the dominant flow determining the penetration to the plasma centre. This is relevant for the question whether the RMP fields will act as a source for neoclassical tearing modes (NTMs). ITER expects to operate the RMP coils in an n=3 or n=4 configuration to minimize the amplitude of the RMP fields that could trigger NTMs.

The response of the plasma to RMP fields can also lead to an amplification of the applied perturbations. This typically occurs when the plasma is close to an MHD stability limit [Liu2010]. In the case of ELM

control, the relevant MHD stability limits are the kink and ballooning limits in the H-mode pedestal. Given the low-n mode numbers of the RMPs, the kink or peeling mode stability limit will be the most relevant for amplification.

In addition to the shielding and amplification of the RMP fields by the plasma, the RMP fields cause a braking of the plasma rotation due to the torques from the perturbed currents, i.e. from 3D JxB forces, and from the Neoclassical Toroidal Viscosity (NTV) [Shaing2008] [Becoulet2009]. For a consistent modelling, both the shielding, amplification and braking needs to be taken into account to determine the self-consistent stationary state in which there is a balance between the shielding of the RMP due to the rotation and the reduction in plasma rotation due to the resonant and non-resonant braking due to the RMPs. In [Lui2012], the linear MHD RMP response calculations, using the MARS-F code, are combined with a toroidal torque balance equation including the JxB and NTV torques to model the RMP penetration and plasma braking in MAST plasmas. The results show that, in MAST, the braking of rotation is strongest for n=3 where over a large fraction of the minor radius the toroidal rotation is reduced to zero. With increasing toroidal mode number, the braking is less strong. The time scales for the plasma braking to reach a stationary state is on the transport-like time scale of 50-100ms. In [Orain2013] the poloidal and parallel flows, including diamagnetic and neoclassical flows in the pedestal, are evolved self-consistently within a non-linear two-fluid reduced MHD model (without NTV braking) using the JOREK code. However, it will be challenging to obtain a truly stationary solutions on the transport time-scale with non-linear MHD codes. It is likely that the self-consistent stationary state solution will be needed as a basis for a first-principle based criterion for the ELM stabilisation.

The cause for the stabilisation of ELM by RMP fields is generally thought to be due to a reduction of the pedestal pressure(gradient) to below to the MHD stability limit, due to additional transport induced by the RMP fields. The next section describes a comparison of the observed plasma perturbations due to the RMP coils with the MHD simulations of the experiment towards a validation of the MHD model in describing the plasma response. In the following sections, the transport induced by the RMP fields is discussed in or detail, both in a fluid description and a fully kinetic model.

**Validation plasma response**

In experiments, the location of the pedestal temperature and density profiles (in real space) is found to depend on the toroidal phase of the applied non-axisymmetric fields. The peak-to-peak displacement of these profiles as the phase is alternated may often exceed 2 cm in typical DIII-D discharges [Moyer2012]. In some cases, the measured displacement is comparable to the displacement of the separatrix manifolds due to the applied fields in the absence of plasma response [Wingen2009,Orlov2012,Shafer2012]. However, in other cases, particularly with n = 1 and n = 2 applied fields in DIII- D, displacements can be much greater than the predictions of vacuum modelling (i.e. without plasma response). For example, in DIII-D discharge 117327 in which a n = 1 field was applied using 2 kA in the DIII-D I-coils, the manifold displacement from vacuum modelling was found to be roughly 0.7 cm, much smaller than the nearly 4 cm measured displacement. This implies that the displacement may be significantly enhanced by the response of the plasma in some cases. In order to investigate the role of plasma response in the measured displacements, calculations of the linear response to applied non-axisymmetric fields have been carried out for several DIII-D discharges using the M3D-C1 code [Jardin2007,Ferraro2010]. M3D-C1 is well-suited for calculating the plasma response in the pedestal, both because it includes the plasma, diverted separatrix, and open-field-line region self-consistently in its computational domain, and because it includes the diamagnetic contributions to the plasma velocity that dominate the E×B flows in the steep

gradient region. These diamagnetic flows have been shown to strongly affect the tearing response of the plasma driven by external perturbations, and tend to reduce the size of islands in the H-mode pedestal considerably [Fitzpatrick1993,Heyn2008,Nardon2010,Ferraro2012]. In particular, it is found that islands tend to be well-screened by the plasma except where the component of the electron rotation perpendicular to the magnetic field is small. These calculations generally find good quantitative agreement with the experimentally measured temperature and density displacements for several DIII-D discharges [Ferraro2013]. For example, in DIII-D discharge 148712, Thomson scattering measurements reveal a displacement of the temperature perturbation resulting from 4 kA of current in the DIII-D I-coils in an even-parity n = 3 configuration reveal a shift of the electron temperature profile along the Thomson chord (R = 1.94 m) of roughly 1 cm when the sign of the I-coil current is flipped. The temperature perturbations from these applied field calculated by M3D-C1 are in relatively good agreement with both the phase and magnitude of these measurements, as illustrated in figure 6. Single-fluid resistive modeling was also found to yield better agreement with experimental measurements than vacuum modeling in this case; however, the inclusion of two-fluid effects and equilibrium rotation were both found to improve the quantitative agreement. The expected helical displacements due to fields from ELM control coils in ITER have also been calculated for several 15MA QDT = 10 scenarios. The magnitude of the displacement was found to increase with the pedestal height and, in contrast with DIII-D results, with toroidal mode number. These trends are thought to be a reflection of the fact that the scenarios under consideration were close to ideal peeling-ballooning stability thresholds, which tend to be less stable at larger n and larger pedestal height. For these cases, the calculated displacements at the midplane were found to range from less than 1 cm (for n = 1 fields applied to a 3.8 keV pedestal scenario) to more than 6 cm (for n = 4 fields applied to a 6.0 keV pedestal scenario) at the maximum designed ELM coil currents (90 kA). Because these displacements are comparable to the equilibrium gradient scale lengths in the pedestal, the validity of the linear approximation used in these calculations is questionable. Indeed, a posteriori analysis of the linear results has found that the linear approximation breaks down in the pedestal for the ITER calculations with displacements larger than roughly 3 cm, and often breaks down in the edge and near mode-rational surfaces for typical DIII-D parameters [Ferraro2013]. In addition, qualitative differences between linear and nonlinear ideal- MHD perturbed equilibria calculated for a typical DIII-D discharge by IPEC [Park2007] and VMEC [Hirshman1983], respectively, indicate that nonlinear effects may be important. Fully nonlinear two-fluid calculations at realistic values of dissipation are extremely numerically challenging, but such recent calculations using M3D-C1 and JOREK [Orain2013] have had some recent success. These calculations will provide a clearer picture of the role of nonlinear effects in the plasma response. A consistent finding of the linear, two-fluid calculations is that the plasma response tends to strongly reduce the resonant components of the perturbed normal field in the H-mode edge, and thus reduces the size of the islands [Schaffer2008], due to the large diamagnetic perpendicular electron rotation in that region. However, for discharges in which the ion rotation is in the co-current direction, the perpendicular electron rotation changes sign near the top of the pedestal (typically near $\psi \approx 0.9$), and in this region the islands are not screened and may be enhanced. This suggests a potential mechanism for ELM suppression by resonant magnetic perturbations (RMP): magnetic stochastization near the top of the pedestal may create a “wall” of transport that does not allow the pedestal to widen to the point of ELM instability [Snyder2012]. Indeed, a recent analysis of a set of DIII-D discharges with applied non-axisymmetric magnetic perturbations has found that the modeled level of stochasticity localized at the pedestal top correlates with ELM suppression better than measures of stochasticity throughout the entire edge that have been considered previously [Fenstermacher2008]. Ultimately, a predictive model of ELM

suppression will likely require a combined understanding of the helical deformations of the plasma in response to the applied fields and of the transport processes arising from these deformations.

**RMP induced transport: fluid model**

In the following, we discuss the effect of an RMP on transport in the case where most of the islands it induces are suppressed, so that island overlap plays a negligible role [Heyn2008, Becoulet2009, Becoulet2012]. This does not rule out the existence of a fully reconnected, isolated islands, such as that which is predicted to occur at the flux surface near the top of the pedestal where the electron rotation reverses [Waelbroeck2003,Heyn2008,Becoulet2013]. In the absence of chaos, the plasma can be divided into three regions: resonant layers containing suppressed islands, non-resonant regions separating the layers, and (possibly) an isolated fully reconnected island. The changes in the profiles caused by the application of a resonant magnetic perturbation can then be attributed to three causes: resonant fluxes caused by the singular response of the plasma near field-line resonances, non-resonant neoclassical fluxes caused by the distortions of the equilibrium, and changes in the spectrum and amplitude of turbulent fluctuations. We consider these three causes in turn.

In singular layers where the RMP is screened by the plasma currents, so that the induced island is narrow, the response of the plasma to the applied field gives rise to non-diffusive transport effects.[Nardon2010,Waelbroeck2012] The best known of these transport effects is the resonant braking that is responsible for the appearance of locked modes. Resonant braking is caused by a non-ambipolar radial current that also results in localized fluxes of particles and heat. In the core, these localized fluxes have a negligible effect. In the edge, by contrast, the strong density and temperature gradients enable the resonant fluxes to cause significant particle and temperature transport. These fluxes can be divided into convective fluxes caused by RMP-induced eddies and "magnetic utter" fluxes, so named because they can be interpreted as resulting from the parallel current along the perturbed magnetic field, i.e. $J_r = (B_r/B)\, J_{||}$. Calculations using reduced isothermal models show that the flutter fluxes strongly dominate the convective fluxes [Waelbroeck2012]. The calculated "braking" forces are consistent with experimental observations, while the particle pump-out is comparable to but smaller than in experiments. Note that the braking changes the electric field so as to reduce the velocity of the electrons. Since the ions are rotating in the opposite direction in the edge, their velocity increases during the application of the RMP, consistent with observations. Similar result are obtained for the transport caused by RMPs away from the resonances.[Callen2012, Callen2012a] In this case the RMP-induced fluxes are much smaller, but they act over a much larger region. Recent calculations for the non-resonant transport have included the thermal transport and find that it dominates over the particle transport by a factor of 3 or so. The relative magnitude of the resonant and non-resonant contributions to RMP-induced heat and particle fluxes is an open question that can only be considered by considering model describing both phenomena consistently.

Lastly, the effects of the RMP on turbulent transport are poorly known both theoretically and experimentally. This question has recently been examined with the help of gyrokinetic simulations of a reconnected magnetic island in a DIII-D equilibrium [Waltz2012]. The simulations confirms that the electron temperature does not fully flatten in the island due to the contribution of trapped particles [Park2010] and that the density steepens in the island for positive radial electric field [Yu2009]. They also find that the force acting on the island scales like the product of the radial electric field, the island width, and the square root of the turbulent intensity. Lastly, they show that when the magnitude of the electric field exceeds a threshold, the island unlocks from the RMP, spins up, and heals until only a suppressed island remains.

## Kinetic simulation of RMP penetration and plasma transport response

In this section, we present a nonlinear kinetic study of self-consistent RMP penetration and plasma transport response, including the radial electric field and plasma rotation responses. The full distribution function (full-f) drift-kinetic particle-in-cell code XGC0 [Park2010] is used. XGC0 includes kinetic ions, kinetic electrons, Monte Carlo neutral particles with ionization and charge exchange cross-sections, plasma loss to the material wall, logical wall sheath, and heat and momentum fluxes from the core plasma. Particle-momentum-energy conserving Monte-Carlo Coulomb collision operator is used for this simulation. Ambipolar anomalous transport is modeled as random walk of marker particles in the radial direction, in addition to the Lagrangian equation of motion in tokamak geometry.

Given the experimental observation that the plasma pressure profile is supported by the magnetic field in the presence of RMPs, we assume that the perturbed 3D magnetic field from RMP coils can only be partially stochastic, that statistically averaged macroscopic plasma quantities (density, temperature, and flow, etc) are function of unperturbed magnetic flux $\psi$, and that the electrostatic potential is also function of the unperturbed magnetic flux, $\Phi(\psi)$, due to strong electrical equilibration along non-stochastic magnetic field component. The last assumption implies that the local electric field along the perturbed magnetic field is described by $E_{\|} = -\mathbf{b}\cdot\nabla\psi d\Phi(\psi)/d\psi$, where **b** is the unit vector in the total local magnetic field direction. It is also assumed that the perturbation in the toroidal component of the magnetic field $B_T$ is negligible due to its rigidness in low plasma $\beta$ (= plasma energy / magnetic field energy). An additional assumption is that the turbulence-driven transport is weaker than the RMP-driven transport. Thus, anomalous transport fluxes are used only to match the plasma profile prior to RMP application.
In the plasma, the perturbed poloidal flux $\delta\psi$ is related to the toroidal component of the perturbed 3D plasma current $\delta j_T$ according to the Ampere's law in a tokamak geometry

$$\Delta^* \delta\psi = \mu_0 I \, \delta j_T / B_{T0} \qquad (1)$$

where $\Delta^*$ is the two-dimensional Laplacian operator in toroidal geometry (conventionally called the Grad-Shafranov operator) $\Delta^*\psi = R\, \partial/\partial R\, [(1/R)\, \partial\psi/\partial R] + \partial^2\psi/\partial Z^2$, $B_{T0}$ is the magnitude of the axisymmetric magnetic field vector $\mathbf{B}_0$ in the toroidal direction, $\mathbf{B} = \mathbf{B}_0 + \delta\mathbf{B}$, $I = RB_{T0}$, and R and Z are the cylindrical coordinates (major radius and vertical distance, respectively). $\delta\psi$ consists of the vacuum RMP part $\delta\psi_v$ and the plasma response part $\delta\psi_p$, $\delta\psi = \delta\psi_v + \delta\psi_p$. Far into the scrape-off plasma ($\psi \geq 1.06$ in this simulation), it is assumed that $\delta\psi_p$ vanishes. Thus, $\delta\psi = \delta\psi_v$ for $\psi \geq 1.06$, forming the boundary condition to Eq. (1). The simulations are started without RMPs until the plasma and rotation profiles qualitatively resemble the experimental profiles under a trial-and-error combination of heating power, torque and anomalous transport rate before turning on the RMP field.

In order to study the basic physics of the RMP penetration and the plasma response processes, we have used one of the original RMP discharge plasmas on DIII-D –Shot number 126006– that exhibited a typical RMP behavior leading to ELM suppression .Figure 7 shows the change of measured pedestal plasma profiles due to RMPs being rather different compared to predictions by the well-known free-streaming model of plasma transport in a stochastic magnetic field by Rechester and Rosenbluth (called R-R theory hereafter) [Rechester1978]. After applying RMPs, experiments observed a strong reduction in the pedestal electron density $n_e$ without reduction in the electron temperature $T_e$, which is opposite to the predicted $T_e$ profile collapse with little effect on the $n_e$ profile from the R-R model. The experimental

observation on the electron particle and thermal transport is more consistent with a recent numerical understanding of stochastic plasma transport in fixed stochastic magnetic field structure [Park2010].

Figs. 7(a) shows the electron transport barrier moving radially outward and narrowing in the close vicinity of the magnetic separatrix after the RMP application. Figure 7(b) and (c) show that the dip in the toroidal rotation profile moves out together with the electron transport barrier and the negative $E_r$ well is preserved to some degree in the vicinity of the separatrix. For a confident extrapolation of the RMP physics to ITER, these peculiar features need to be understood self-consistently from each other in a kinetic study that can simulate the RMP penetration, plasma transport response, radial electric field, and the toroidal rotation together.

In this kinetic study even parity vacuum RMPs from 4kAt I-coil coil current is used. In order to match approximately the plasma temperature, density, and rotation profiles between the simulation and experimental results prior to the start of RMPs, 6 MW of total heat flux from the core plasma is evenly divided into ions and electrons at the core-edge boundary ($\psi_N$=0.8), together with 4 N-m of toroidal torque. These values are somewhat lower than the total heating power and the total neutral beam torque into the plasma in the experiment. Effective radial anomalous transport coefficients at the level of $D_{eff}=\chi_e=\chi_i=0.2$ $m^2/s$ is found to be adequate for this qualitative study.

Figure 8 shows the density, $T_e$ and $T_i$ profiles before (black) and 4ms after (red) the start of RMPs from the XGC0 simulation. $\psi_N$ is the normalized poloidal magnetic flux. It can be seen that most of the hard-to-understand features observed in the experimental electron density and temperature plasma profiles, as summarized earlier, are reproduced in the simulation results: the density pump-out and the radially outward movement of the steep $T_e$ region. Also shown in Figure 8 is the radial electric field profile before (black) and 4ms after (red) RMPs. It can be seen that the strong $E_r$xB shearing remains at larger minor radii near the magnetic separatrix surface. The toroidal rotation also behaves qualitatively similarly to the experimental behaviour (Fig. 7(b)).

In-depth investigation of the physical processes reveals that the vacuum stochasticity and islands are suppressed by the plasma response at the outer part of the original pedestal layer just inside the separatrix surface. However, at the inner part from that layer, the stochasticity and islands are recovered to the vacuum level by the plasma response. As a result, the pedestal top is extended radially outward by RMPs until the RMP suppression layer is reached. Figure 8 shows the resonant components m=8-14 in vacuum (black) and in plasma (red) at the resonance radii for each component. Suppression of the outer most resonant components (m=12 and 13) and amplification of the inner resonant components back to the vacuum level can be noticed. Regardless of the initial condition, the perpendicular electron rotation self-organizes to be small in the amplification region and large in the suppressed region, consistently with the theoretical MHD insight presented above.

Next, we study the effect of plasma safety factor q on the RMP penetration. It has been experimentally known from DIII-D [Evans2004,Burell2005] that there is a "$q_{95}$-window," inside which the RMPs act to stabilize ELMs even though the vacuum RMP distribution is similar inside or outside of the $q_{95}$-window. Understanding the dependence of RMP penetration on $q_{95}$ is important for ITER operation since the existence of the $q_{95}$-window indicates that the ELM suppressibility by RMPs could be sensitive to the $q_{95}$ value. In XGC0, the global safety factor q profile is varied by multiplying a constant number to the toroidal magnetic field strength. Figure 9 shows the radial distribution of Chirikov parameter at three different $q_{95}$ values: $q_{95}$=3.47, 3.58, and 3.69. The value 3.58 is inside the $q_{95}$ window and the other two values are outside. The vacuum Chirikov profile is similar for all three cases. But the plasma responded RMP profile is different inside the $q_{95}$-window. When $q_{95}$ is inside the ELM suppression window (red

diamonds), there is a stronger stochastic connection between pedestal top to scrape-off layer/divertor plate.

Other studies performed include the effect of electron collisionality, density, and toroidal plasma rotation on the RMP penetration and pedestal transport response. ELM suppression on DIII-D has been reliable at ITER relevant low electron collisionality ($\nu_{e*}$~0.1). However, such a low collisionality has been achieved in DIII-D only at factor of two lower electron pedestal density than the predicted ITER level. When the pedestal electron density is raised to an ITER-relevant level, the reliability of ELM suppression is lost. Since the increase in pedestal density is accompanied by decrease in pedestal $T_e$ and, thus, by an order of magnitude rise in the pedestal collisionality, we need to know if the loss of the ELM suppression in DIII-D is caused by the higher collisionality or by higher density. For this study, we have first multiplied the collision operator by a constant acceleration factor, while keeping the initial density and temperature profile the same. Figure 10 shows the dependence of the Chirokov parameter profile on the electron collisionality. A sharp decrease in the stochastic connection between pedestal top and divertor plate can be seen as the collisionality increases by factor of 10. This is a similar stochasticity behavior as in the "outside $q_{95}$-window" case. Using the stochasticity behavior as an indication for ELM suppressibility, as indicated from our limited study, we could conclude that 10 times higher electron collisionality takes the RMPs outside the ELM suppression window. Since the stochasticity and islands are suppressed throughout the entire pedestal region, little change in the pedestal plasma profile has resulted, as observed in DIII-D experiment. On the other hand, an increase by a factor of 2 in the electron density to an ITER relevant level, while keeping the electron collisionality at ITER relevant level, gives only an insignificant amount of change in the Chirikov parameter profile. Thus, it appears that the ELM suppression scheme from DIII-D is relevant to ITER even though the experimental scheme cannot be confirmed at an ITER relevant pedestal density level.

The next study we present is the sensitivity of the RMP penetration on plasma rotation. A 50% reduction in the toroidal rotation speed shows a relatively insignificant effect on the Chirikov parameter profile in the pedestal area, while it shows a more significant effect toward the core plasma. Strong reduction in Chirikov parameter from 50% higher toroidal rotation in the core side is consistent with insight from the linear MHD theory. However, in the edge confinement barrier area, where a strongly sheared ExB rotation exists, the toroidal rotation shows a non-dominant effect on the Stochasticity and islands. In the edge of a tokamak including ITER, spontaneously generated rotation by the edge effect should be dominant over the externally driven rotation. Thus, the present study suggests that the low externally driven toroidal rotation speed predicted in the core of ITER is not expected to affect the edge RMP penetration at a significant level.

More detailed studies on extended experimental data set, including results from other tokamak devices, and on an the actual ITER plasmas are needed for a more complete understanding of the RMP effect on ELM suppression in ITER plasmas.

## ELM Control methods: Pellet Pacing

A well-established method for the control of the ELM frequency, and thereby the ELM energy loss, is the injection of pellets into the H-mode pedestal region (ELM pellet pacing). First observed in AUG [Lang2004], pellet pacing is now a reliable method for ELM frequency control in JET [Lang2011, Lang2013], AUG [Lang2008], DIII-D [Baylor2013, Baylor2013a]. Recently, ELM pacing experiments in DIII-D have demonstrated an increase of the natural ELM frequency by a factor of 12 and a corresponding reduction in energy loss per ELM. A question remains on the efficiency of pellet pacing in reducing the peak heat flux of the ELMs at the divertor. In JET [Lang2013] pellet pacing experiments it is observed that, although the total energy loss per ELM decreases with increasing ELM frequency, the peak power flux onto the target does not decrease significantly. This is in contrast to the results from DIII-D experiments [Baylor2013] where it is found that the peak heat flux during pellet triggered ELMs scales with the inverse of the pellet pacing frequency.
ITER will have 6 pellet injectors for the combined use of fuelling and ELM control. The pellets can be injected from the low-field side, above the x-point and from two locations on the high field side. The requirements on the pellet size and speed for ELM pacing have been derived from the observation [Kocsis2007, Lang2011] that the pellet needs to reach the top of the H-mode pedestal to reliably trigger an ELM [Polevoi2008,Gal2008]. For a more detailed derivation of the required pellet parameters, a physics model for the onset of the pellet triggered ELM is needed. This physics model will need to be validated against current experiments.

The non-linear MHD code JOREK [Huijsmans2009] has been extended to include a model for the density source coming from the ablation of an injected Deuterium pellet [Futatani2014]. The pellet is assumed to travel along a straight line with a given fixed velocity. The amplitude of the space and time varying density source, is such that the integrated source rate is consistent with the NGS pellet ablation model [Gál2008a]. Due to limitations on the grid resolution the pellet density source rate is assumed to be spread over a significantly wider region in space.
The results of the non-linear MHD simulations of pellet injection into an, initially MHD stable, H-mode pedestal lead to the following model for the pellet trigger of an ELM. The ablation of the pellet as it travels into the plasma causes a large local, moving density source. Since the deuterium pellet injection is mostly adiabatic, initially, the temperature at the location of the density source will drop such that the local pressure stays constant. At this initially constant pressure, there is no parallel pressure gradient driving a parallel flow of the density perturbation. Due to the large electron heat conductivity, the density perturbation will be quickly heat up. This will result in a local pressure maximum which will cause the density perturbation to spread in the parallel direction with the local sound speed. Due to faster parallel heating time compared to the ion-sound transit time, the local pressure perturbation can be significant (see below). The resulting 3D high pressure structure can in principle destabilize ballooning modes, even if the 2D axi-symmetric pressure profile remains below the ballooning stability limit. The destabilisation of a ballooning mode by this 3D pressure perturbation has been proposed as the trigger for the ELM by a pellet.
The amplitude of the 3D pressure perturbation depends on parallel heat transport into the high density cloud. In an unperturbed axisymmetric plasma, the volume connected by field lines to the pellet cloud is determined by the flux surface and the radial width of the pellet. However, the MHD simulations [Huysmans2009, Futatani2014] show that the 3D pellet perturbation causes a significant magnetic

perturbation leading to an ergodic layer around the pellet cloud. This increases the magnetically connected volume and the amount of energy available to heat the pellet cloud.

Simulations of pellet injection in DIII-D plasmas have shown that the amplitude of the pressure perturbation created by the pellet must exceed a critical value in order to trigger a ballooning-type instability (leading to an ELM). This critical pressure perturbation implies that a minimum pellet size is necessary to trigger an ELM. Figure 11 shows the perturbed pressure profile in the mid-plane in DIII-D for different pellet size, either at the time of the maximum perturbation or at the time of the onset of an MHD instability. It shows that the onset of the MHD instability occurs at the same level of perturbed pressure independent of the pellet size (as long as the pellet size is above the minimum size). The required pressure perturbation is about 2.5 times above the pressure at the top of the pedestal. The minimum pellet size needed for ELM trigger can now be predicted from simulations. For a DIII-D ITER-like plasma, with pellet injection at the mid-plane, the predicted minimum pellet size is 1.3mm ($8.6 \times 10^{19}$ atoms). Recent experiments in DIII-D [Baylor2014] have established a critical pellet size at $3.5 \times 10^{19}$ atoms, a factor 2.5 below the predicted value. The difference is likely due to the larger volume of the density source in the simulations compared to the experimental pellet cloud, due reasons of achievable numerical resolution.

The MHD simulations show that the minimum pellet size depends on the pellet injection geometry. Injection from the high field side triggers instability at smaller pellets compared to low field side midplane injection [Futatani2014]. Injection close to the x-point on the low field side (i.e. one of the ITER injection geometries) requires a minimum pellet size between the LFS and HFS pellet size.

The predictions for ITER for a Q=10 H-mode plasma at 15MA, a minimum pellet size $2 \times 10^{21}$ atoms for X-point injection, are consistent with earlier estimates based on the criterion that the pellet needs to reach the top of the pedestal. Given the ratio of predicted to observed minimum pellet size in DIII-D, the prediction for ITER is an upper estimate.

The MHD simulations of pellet triggered ELMs in DIII-D, JET and ITER geometry, consistently show a second peak in the power to the divertor with a characteristic n=1 spiral structure, in addition to an increase in the power to the main strike points. This n=1 structure has been observed in JET experiments [Wenninger2011] but not in AUG or DIII-D. Given that the location of the secondary peak is fixed for a given pellet injection location and magnetic geometry of the plasma, this may lead to a local increase in the divertor erosion. Important questions remain on the broadening of power deposition profile at the divertor as a function of the size of pellet triggered ELMs. Observations in AUG and JET suggest a reduced efficiency of the ELM mitigation due to a reduction in the width of the power deposition profile with an increase of the ELM frequency [Lang2013]. Recent results in DIII-D also find an increase of the width with ELM size [Baylor2014]. Further MHD simulations are necessary to investigate whether the broadening of the ELM power deposition is the same for natural ELMs [Huijsmans2013] and pellet triggered ELMs.

An important aspect of the pellet triggered ELMs for ITER is the amount of density loss due to a triggered ELM. The particle throughput in ITER is limited by the pumping capability at 200 $Pam^3/s$. In case the particle loss per ELM is larger than the number of particles in the injected pellet, the ELM control could consume a large part of the available particle throughput. Assuming a relative density loss $\delta N/N \sim 1\%$ per ELM, at a controlled ELM frequency of 45Hz would lead to a particle flux of $75 Pam^3/s$, significantly reducing the available core fuelling. One solution may be the injection of the ELM control pellets on the high field side. Experiments in DIII-D show a net pellet fuelling [Baylor2014a] for high field side ELM pellet pacing. Also, the ELMs appear to be more easily triggered for high field side

injection [Lang2013]. These observations are consistent with the results from the non-linear MHD simulations. With high field side injection, the ballooning modes are triggered in the region of the unstable negative pressure gradient of the 3D pressure perturbation, i.e. on the inward side of the pressure perturbation. The ballooning modes cause a convection pattern which is directed towards larger major radii. For LFS injection, this implies that density is moved out of the plasma. On the contrary, on the HFS this yields an inward convection of the density [Huijsmans2010]. This may be the cause for the observed net fuelling for HFS pellet pacing. As mentioned above, HFS injection also has the lowest requirements on the minimum pellet size needed to trigger an ELM.

An alternative trigger mechanism was proposed in [Hayashi2013]. From 2D transport modelling it was concluded that the axisymmetric pressure profile steepens locally due to the energy absorption of the pellet, leading to a destabilisation of a ballooning instability. However, the resulting change in the 2D axi-symmetric pressure profile appears to be small compared to the 3D localised pressure perturbation described above. In addition, the time scale for equilibration of the pressure will be several ion-sound transit times as the 3D pressure perturbation propagates in the parallel direction with the local sound speed. This should give a significant time delay to the ELM trigger following the pellet injection if the trigger depends on the 2D equilibration of the pressure profile.

## Conclusions

Increasingly detailed numerical simulations have contributed to a steadily improving understanding of the physics of ELMs and the methods for their control. The current status is at the level of a qualitative and in some cases quantitative description of the phenomena. The EPED model, predicting the height and width of the H-mode pedestal, is a good example of an existing quantitative model, having been validated on a large database including multiple machines. Other examples include the comparison of the predicted plasma response with measured perturbed equilibrium profiles due to RMP fields. Quantitative predictions, for example for amplitudes of ELM energy and particle losses, RMP fields required for ELM stabilisation and pellet requirements for ELM triggering are still being development. These are essential for the validation of the physics models and for extrapolation to future devices such as ITER.
The basic physics model used for the modelling of ELMs and ELM control is the MHD model. However it is clear that the MHD model needs to be extended for a more accurate description of the experimental observations and predictions for ITER. Simulations of multiple ELM cycles will need to include a detailed description of the interaction of the plasma with the divertor, likely including a description of neutrals and impurities (necessary to describe the high recycling ITER divertor). A description of (heavy) impurities is needed to model the effects of ELMs on the impurity concentration and vice-versa. Predictive RMP simulations will need an accurate model for neo-classical physics including neo-classical toroidal viscosity and a (fluid) model for the RMP induced transport combined with non-linear MHD. Alternatively, gyro-kinetic models including a consistent magnetic response with a consistent time-varying equilibrium can be used (but reaching a truly stead-state solution will be challenging). These extensions to the MHD model are essential for the next steps towards a fully predictive model of ELMs and ELM control.

Prepared by LLNL under Contract DE-AC52-07NA27344.

## References


[Aiba2010] N. Aiba et al., Nucl. Fusion 50 (2010) 045002 (1pp)

[Aiba2011] N. Aiba et al., Nucl. Fusion 51 (2011) 083012 (9pp)

[Baylor2013] L. Baylor et al., PRL 110, 245001 (2013)

[Baylor2013a] L. Baylor et al., Phys. Plasmas 20, 082513 (2013)

[Baylor2014] L. Baylor et al., PSI Conference 2014, to appear in Journal Nucl. Mat.

[Becoulet2009] M. Becoulet, et al., Nuclear Fusion 49 (2009) 085011 (13pp)

[Becoulet2012] M. Becoulet, et al., Nuclear Fusion 52 (2012) 054003.

[Boom2011] J.E. Boom, Nucl. Fusion **51** (2011) 103039 (9pp)

[Boozer1983] A. H. Boozer, Phys. Fluids **26**, 1288 (1983)

[Burckhart2013] A. Burckhart, *Different ELM regimes at ASDEX Upgrade and their linear stability analysis*. Dissertation, LMU München (2013)

[Burrell2005] K. H. Burrell, *et al*., Plasma Phys. Controlled Fusion {\bf 47}, B37 (2005)

[Callen2012] J.D. Callen, et al., Nuclear Fusion 52 (2012) 114005

[Callen2012a] J.D. Callen, et al., Physics of Plasmas 19 (2012) 112505

[Canik2010] J. M. Canik et al Nucl Fusion 50(2010) 034012

[Czarny2008] O. Czarny and G. Huysmans, J. Comp. Phys., Vol. 227, Issue 16, (2008) p. 7423-7445

[Degeling2003] A.W. Degeling *et al.*, Plasma Physics and Controlled Fusion **45** (2003), 1637

[Daly2012] E.F. Daly et al., Fusion Science and Technology, Vol. 64 AUG. 2013

[Dudson2011] B.D. Dudson et al., Plasma Phys. Control. Fusion 53 054005 (2011)

[Dudson2009] B. D. Dudson et al., Comput. Phys. Commun. 180, 1467 (2009)

[Eich2011] T. Eich et al., Journal of Nuclear Materials 415 (2011) S856–S859

[Evans2004] T. E. Evans et al., Phys. Rev. Lett. **92**, 235003 (2004)

[Enavs2008] T.E. Evans et al., Nucl. Fusion 48 (2008) 024002

[Evans2013] T.E. Evans et al., Nucl. Fusion **53** (2013) 093029 (13pp)

[Fenstermacher2008] M. E. Fenstermacher et al., Phys. Plasmas 15, 056122 (2008)

[Fenstermacher2013] M.E. Fenstermacher et al. Journal of Nuclear Materials 438 (2013) S346–S350

[Ferraro2010] N. M. Ferraro, S. C. Jardin, and P. B. Snyder, Phys. Plasmas 17, 102508 (2010)

[Ferraro2012] N. M. Ferraro, Phys. Plasmas 19, 056105 (2012).

[Ferraro2013] N. M. Ferraro, et al., Nucl. Fusion 53 (2013) 073042 (8pp)

[Fitzpatrick1998] R. Fitzpatrick, Phys. Plasmas, Vol. 5, No. 9, (1998)

[Fitzpatrick2008] R. Fitzpatrick, Nucl. Fusion 33, 1049 (1993)

[Fischer2012] R. Fischer et al., Plasma Phys. Control. Fusion 54 115008 (2012)

[Futatani2014] S. Futatani et al., Nucl. Fusion **54** (2014) 073008 (20pp)

[Gál2008] K. Gál et al., 21th IAEA Fusion Energy Conference, Chengdu (2006), paper TH/P4-5

[Gál2008a] K. Gál et al., Nucl. Fusion 48 (2008) 085005

[Groebner2010] R.J. Groebner et al  Nucl. Fusion 50 064002 (2010)

[Groebner2013] R.J. Groebner et al., Nucl. Fusion 53 093024 (2013)

[GuoPoP2014] H. Y. Guo, et al, *Phys. Plasmas* **21**, 056107 (2014)[Jardin2007] S. C. Jardin, J. Breslau, and N. Ferraro, J. Comp. Phys. 226, 2146 (2007).

[Jeon2012] Y. M. Jeon et al  Phys. Rev. Lett. 109(2012)035004

[HahmNF2013] T.S. Hahm, Nucl. Fusion 53 (2013) 104026.

[Halpern2011] F.D. Halpern et al., Physics of Plasmas 18, 102501 (2011)

[Hastie2000] R. J. Hastie et al., Phys. Plasmas 7, 4561 (2000)

[Havlickova2012] E. Havlickova et al., Plasma Phys. Control. Fusion **54** (2012) 045002 (21pp)

[Hayashi2013] N. Hayashi et al., 2013 Nucl. Fusion 53 123009
[Heyn2008] M. F. Heyn et al., Nucl. Fusion 48, 024005 (2008)
[Hirshman1983] S. P. Hirshman and J. C. Whitson, Phys. Fluids 26, 3553 (1983)
[Huysmans2001] G.T.A. Huysmans, Phys. Plasmas 8 , 4292 (2001)
[Huysmans2005] G.T.A. Huysmans, Plasma Phys. Control. Fusion, **47** (2005) 12, 2107-2121
[Huysmans2007] G.T.A. Huysmans and O. Czarny, Nucl. Fusion **47** (2007) 659–666
[Huysmans2009] G.T.A. Huysmans et al., Plasma Phys. Control. Fusion **51** (2009) 124012 (14pp)
[Huysmans2010] G.T.A. Huysmans et al., 23th IAEA Fusion Energy Conference, Korea (2010)
[Huijsmans2013] G.T.A. Huijsmans and A. Loarte, Nucl. Fusion 53 (2013) 123023 (10pp)
[KimNF2014] Kim, Minwoo; Choi, Minjun; Lee, Jaehyun; Yun, Gunsu; Lee, Woochang; Park, Hyeon; Domier, C; Luhmann, Neville; Xu, Xueqiao, accepted by Nuclear Fusion 2014.
[Kirk2011] A. Kirk et al., Plasma Phys. Control. Fusion **53** (2011) 065011 (18pp)
[Kirk2012] A. Kirk et al., Phys. Rev. Lett. 108(2012) 255003
[Kleva2007] R.G. Kleva and P.N. Guzdar, Phys. Plasmas **14**, 012303 (2007)
[Knoll1993] D.A. Knoll, A.K. Prinja, and R.B. Campbell, J. Comp. Phys. **104**, (1993) 418
[Kocsis2007] G. Kocsis et al., Nucl. Fusion 47 (2007) 1166–1175
[Lang2004] P.T. Lang et al., Nucl. Fusion 44 (2004) 665–677
[Lang2008] P.T. Lang et al., Nucl. Fusion 48 (2008) 095007
[Lang2011] P.T. Lang et al., Nucl. Fusion 51 (2011) 033010 (16pp)
[Lang2013] P.T. Lang et al., Nuclear Fusion 53 (2013) 073010
[Leonard2002] A W Leonard, et al., Plasma Physics and Controlled Fusion, 44(6):945, 2002
[Leonard2006] A.W. Leonard et al., Plasma Phys. Control. Fusion **48** (2006) A149–A162
[Liang2007] Y Liang et al., PRL 98 265004 (2007)
[Lichtenberg1992] A. J. Lichtenberg and M. A. Lieberman, *Regular and Chaotic Dynamics*, 2nd ed. (Springer-Verlag, New York, NY, 1992)
[Liu2010] Y.Q. Liu et al., Phys. Plasmas **17**, 122502, (2010)
[Liu2012] Y.Q. Lui et al., Plasma Phys. Control. Fusion **54** (2012) 124013
[Loarte2014] A. Loarte et al. Nucl. Fusion **54** (2014) 033007 (18pp)
[MaNF2014] J.F. Ma, X.Q. Xu, and B.D. Dudson, *Nucl. Fusion* **54,** 033011 (2014)
[Moyer2012] R. A. Moyer, et al., Nucl. Fusion 52, 123019 (2012)
[Maruyama2010] S. Maruyama et al., 23th Fusion Energy Conference (2010), Daejong, paper ITR/P1-28
[Nardon2010] E. Nardon, et al., Nucl. Fusion 50, 034002 (2010)
[Orlov2012] D. M. Orlov, et al., Fusion Eng. and Design 87, 1536 (2012)
[Pacher2011] H.D. Pacher et al., Journal of Nuclear Materials 415 (2011) S492–S496
[Pamela2011] S. Pamela et al., Plasma Phys. Control. Fusion **53** (2011) 054014
[Pamela2013] S. Pamela et al., Plasma Phys. Control. Fusion **55** (2013) 095001 (13pp)
[Pankin2007] A.Y. Pankin et al., Plasma Phys. Control. Fusion, 49(7):S63, 2007
[Park1999] W. Park, et al., Phys. Plasmas **6**, 1796 (1999)
[Park2007] J.-K. Park, A. H. Boozer, and A. H. Glasser, Phys. Rev. Lett.14, 052110 (2007)
[Park2010] G. Park, et al., Physics of Plasmas 17 (2010) 102503
[Park2012] H.K. Park et al., IAEA Fusion Energy Conf. 2012, San Diego, USA, paper EX/11-3
[Polevoi2008] A. Polevoi et al., 35th EPS Conference on Plasma Phys. Hersonissos, ECA Vol.**32D**, P-1.109 (2008)
[Rechester1978] A.B. Rechester and M.N. Rosenbluth, Phys. Rev. Lett. **40** (1978) 38

[Roeder03] R.K.W. Roeder, B.I. Rapoport, and T.W. Evans, Phys. Plasmas **10**, 3796 (2003)
[Saarelma2005] S. Saarelma et al., Plasma Phys. Control. Fusion 47 (2005) 713–731
[Saarelma2007] S. Saarelma et al., Plasma Phys. Control. Fusion **49** (2007) 31–42
[Saarelma2011] S. Saarelma et al., Plasma Phys. Control. Fusion **53** (2011) 025011 (11pp)
[Saarelma2012] S. Saarelma et al., Nucl. Fusion **52** (2012) 103020 (7pp)
[Saarelm2013] S. Saarelma et al., Nucl. Fusion **53** (2013) 123012 (9pp)
[Scannell2013] R. Scannell et al., Plasma Phys. Control. Fusion 55 (2013) 035013
[Schafer2012] M. W. Shafer et al., Nucl. Fusion 52, 122001 (2012)
[Schaffer2008] M. J. Schaffer,et al., Nucl. Fusion 48, 024004 (2008)
[Shaing2008] K.C. Shaing et al., Phys. Plasmas **15**, 082506 (2008)
[Snyder2004] P.B. Snyder et al., Nucl. Fusion 44 (2004) 320–328
[Snyder2007] P.B. Snyder et al., Nucl. Fusion 47 (2007) p. 961-968
[Snyder2011] P.B. Snyder et al., Nucl. Fusion **51** (2011) 103016 (8pp)
[Snyder2012] P. B. Snyder et al., Phys. Plasmas 19, 056115 (2012)
[Sugiyama2000] L. E. Sugiyama and W. Park, Phys. Plasmas **7**, 4644 (2000)
[Sugiyama2009] L. E. Sugiyama and the M3D Team, J. Phys.: Conf. Ser. **180**, 012060 (2009)
[Sugiyama2010] L. E. Sugiyama and H. R. Strauss, Phys. Plasmas **17**, 062505 (2010)
[Sugiyama2012] L. E. Sugiyama, Physica Scripta **86**, 058205 (2012)
[Suttrop2011] W. Suttrop et al., 2011 Phys. Rev. Lett. 106 225004
[Thyagaraja2010] A. Thyagaraja et al., Phys. Plasmas **17**, 042507 (2010)
[Tskhakaya2009] D. Tskhakaya et al., Journal of Nuclear Materials 390–391 (2009) 335–338
[Waelbroeck2003] F.L. Waelbroeck, Phys. of Plasmas 10 (2003) 4040.
[Waelbroeck2012] F. Waelbroeck, et al., Nuclear Fusion 52 (2012) 074004
[Waltz2012] R. E. Waltz, et al., Physics of Plasmas 19 (2012) 032508
[Wenninger2011] R. Wenninger et al., NUcl. Fusion 53, (2011) 105002
[Wingen2009] A. Wingen, T. E. Evans, and K. H. Spatschek, Nucl. Fusion 49, (2009) 055027
[Xi2012] P.W. Xi et al., Phys. Plasmas 19 092503 (2012)
[Xi2013] P.W. Xi, X.Q. Xu, T.Y. Xia, W.M. Nevins and S.S. Kim, *Nuclear Fusion* Volume **53,** 11 (2013)
[XiPoP2014] P. W. Xi, X. Q. Xu and P. H. Diamond*, Phys. Plasmas* **21**, 056110 (2014)
[XiPRL2014] P. W. Xi, X. Q. Xu and P. H. Diamond, *Phys. Rev. Lett.* **112**, 085001 (2014
[Xia2012] T.Y. Xia et al., Contrib. Plasma Phys. 52 353 (2012)
[Xia2013] T.Y. Xia and X.Q. Xu, Phys. Plasmas, 20, 052102 (2013)
[Xia2013a] T.Y. Xia, X.Q. Xu and P.W. Xi, Nucl. Fusion 53 (2013), 073009
[Xu2010] X.Q. Xu etal., 2010 Phys. Rev. Lett. 105 175005
[Xu2011] X.Q. Xu et al., Phys. Rev. Lett. 105 175005 (2010)
[Xu2011a] X. Q. Xu et al., Nucl. Fusion 51 103040 (2011)
[Xu2013] X. Q. Xu et al., Phys. Plasmas 20, 056113 (2013)
[Yu2009] Q. Yu, et al., Nuclear Fusion 49 (2009) 062001 (5pp)
[Yun2011] G.S. Yun et al., PRL 107, 045004 (2011)

## Figures

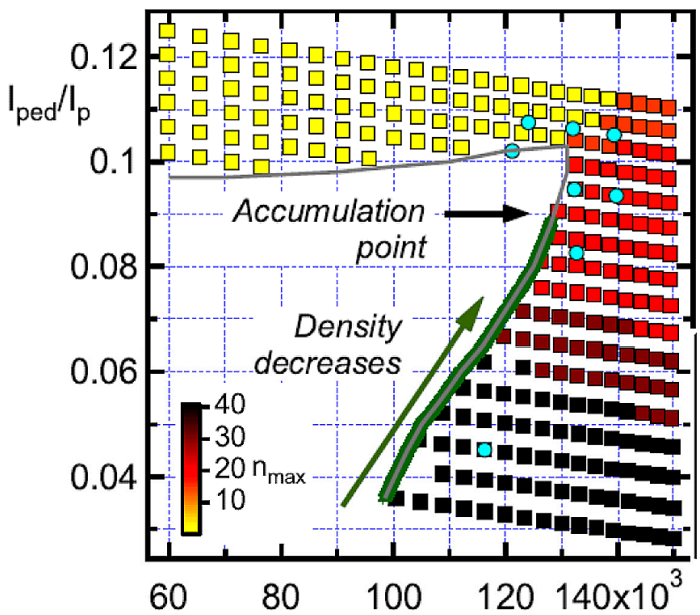


***Figure 1*** *Ideal MHD stability limits of the edge pedestal for an ITER Q=10 equilibrium including toroidal mode numbers n=3-40. The green curve indicates the stability limit as a function of the pedestal density.*

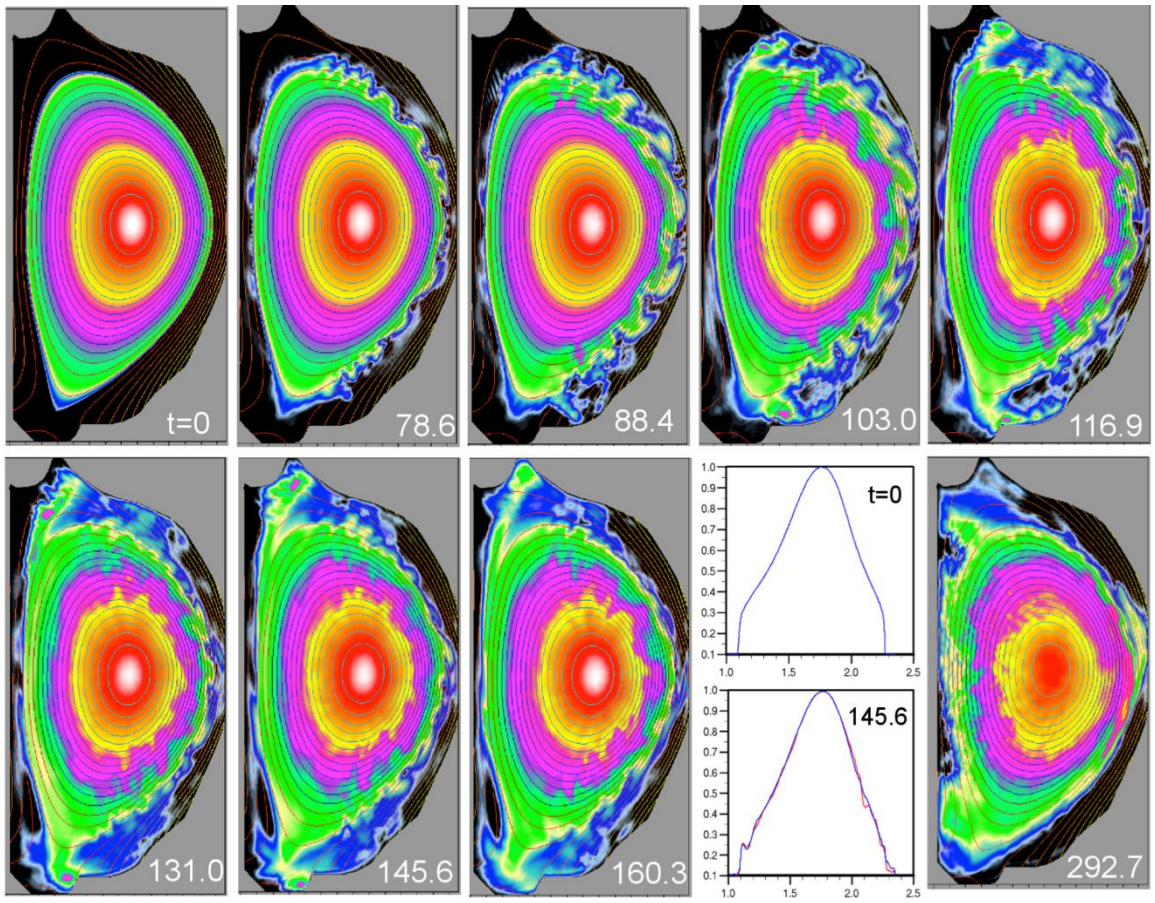


***Figure 2***. *Density contours in vertical cross-section over the ELM crash and saturation of outboard instability for case of Fig. 1 with no background toroidal rotation.*
*Times in units of shear Alfvén times (1 $\tau_A \approx 0.5\mu s$). Figure from [Sugiyama2012].*

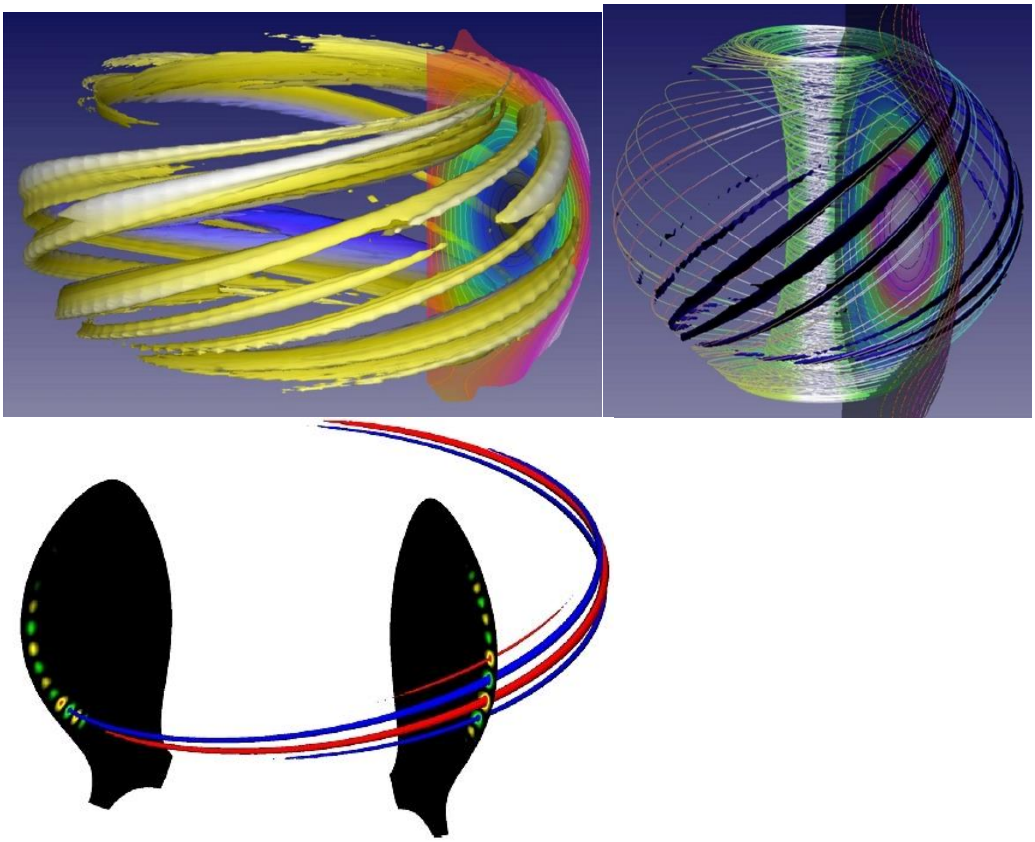

*Figure 3*

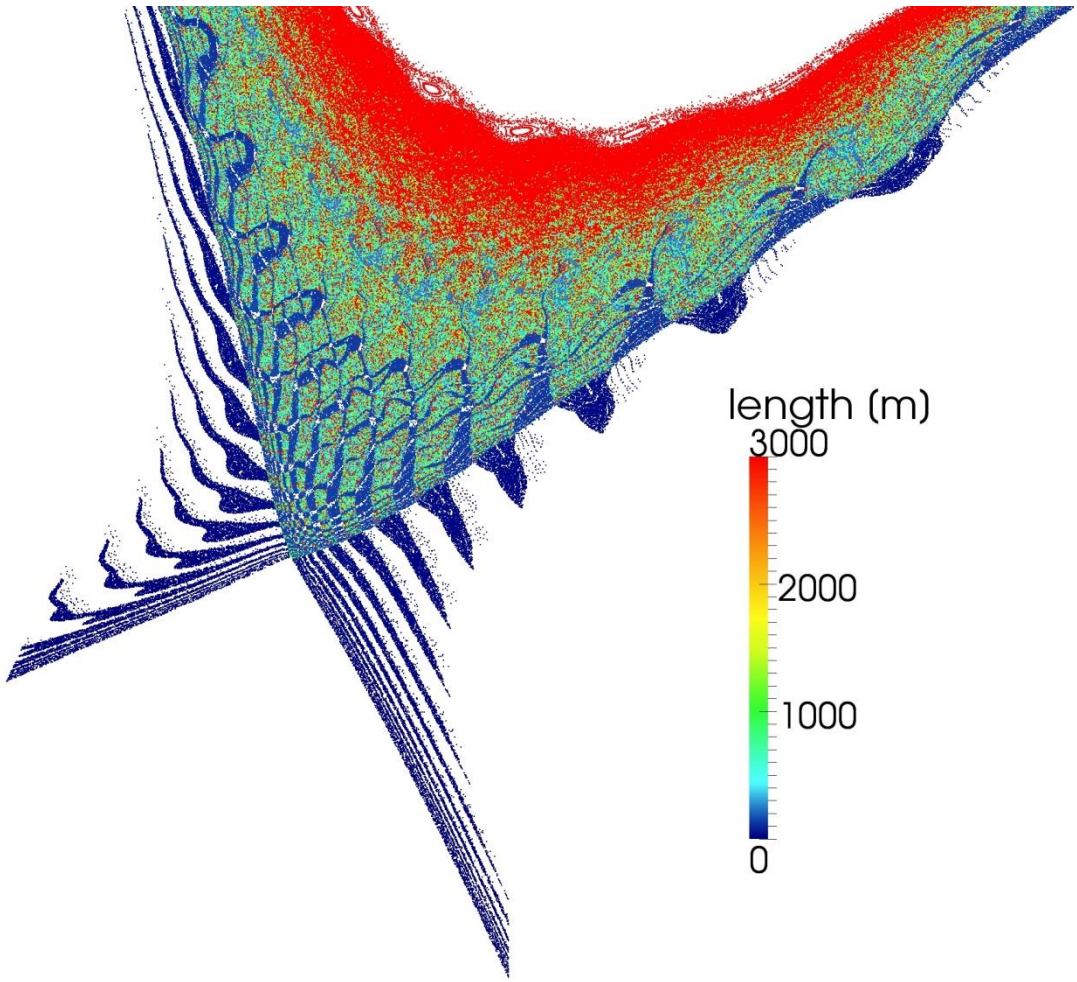


***Figure 4*** *A Poincare plot of the magnetic field, showing the magnetic tangles at the time of the maximum magnetic perturbation during an simulated ELM in ITER.*

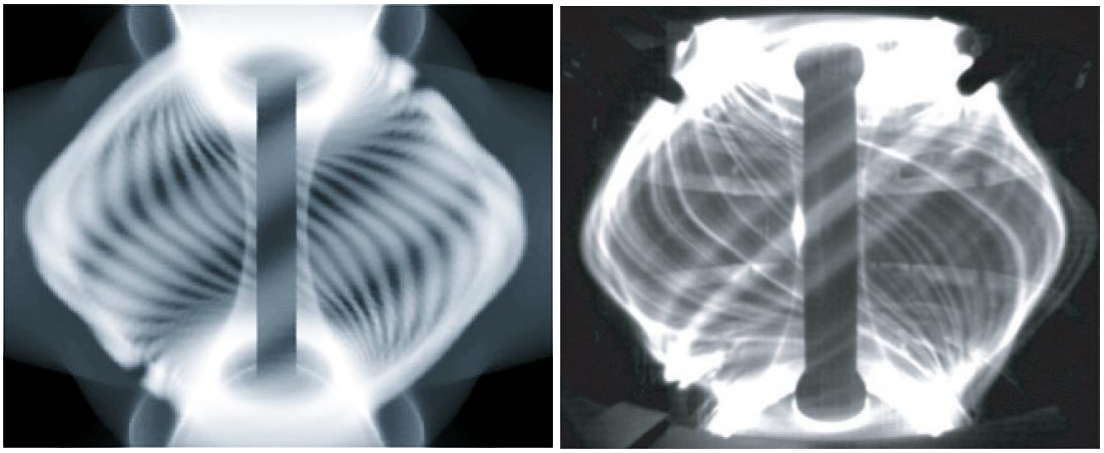

***Figure 5*** *Comparison of visible camera image of an ELM in MAST (right) with the predicted image from non-linear MHD ELM simulation [from Pamela2013]*

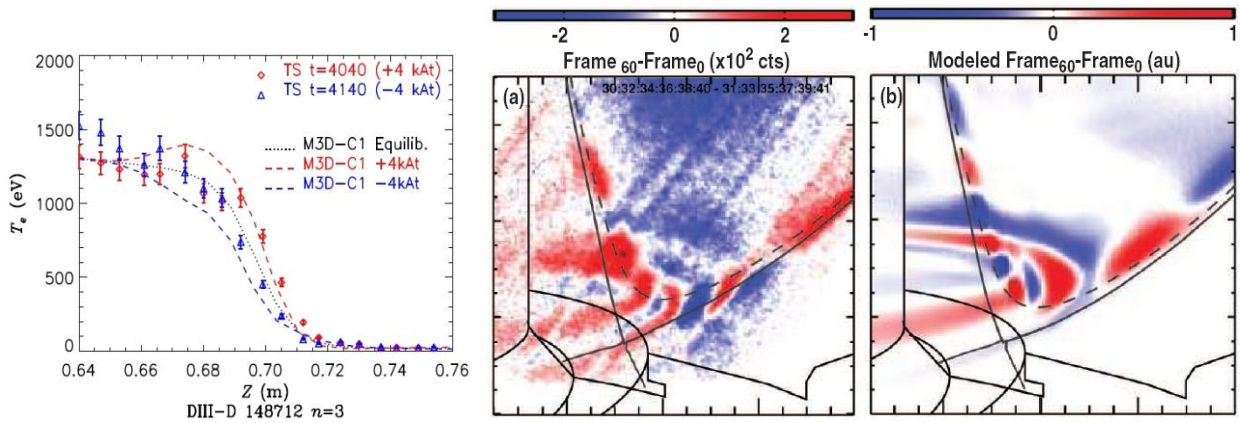


***Figure 6****. Left: Electron temperature measured by Thomson scattering (symbols) and calculated by M3D-C1 (dashed lines) with even-parity n = 3 fields applied by +4 kA (red) and -4 kA (blue) in the DIII-D I-coils. Middle: the difference between SXR signal measured with even-parity n = 3 fields applied by +4 kA (red) and -4 kA (blue) in the DIII-D I-coils. Right: The simulated differential SXR signal from the M3D-C1 calculation [**add reference**].*

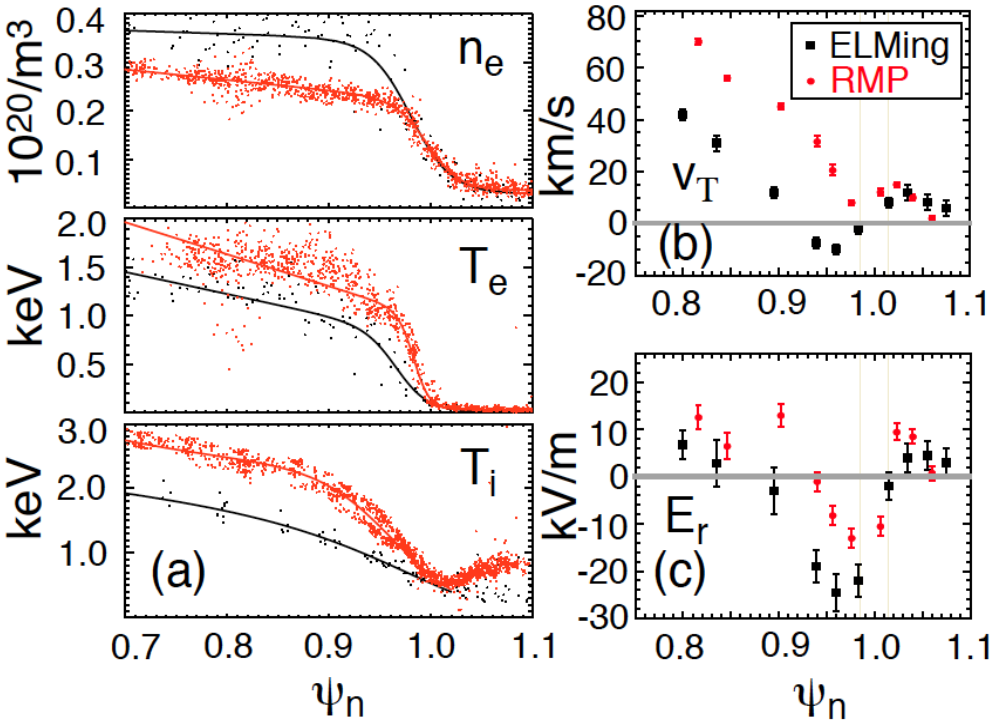


***Figure 7*** *Experimentally observed changes in (a) n, $T_e$ and $T_i$ pedestal profiles, (b) toroidal rotation, and (c) radial electric field before (black) and after (red) the RMP application on DIII-D discharge 126006. This figure is from Ref. [Park2010]. Notice opposite color designations from Fig.8.*

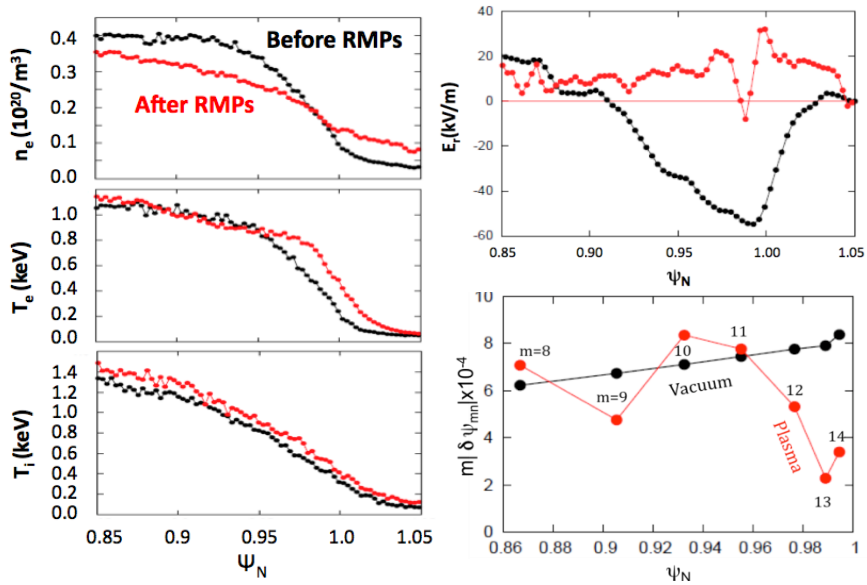


***Figure 8*** *Plasma profile changes (density, electron and ion temperature, radial electric field and resonant perturbed magnetic flux) before (black) after (red) 4ms of RMP penetration from XGC0 simulation.*

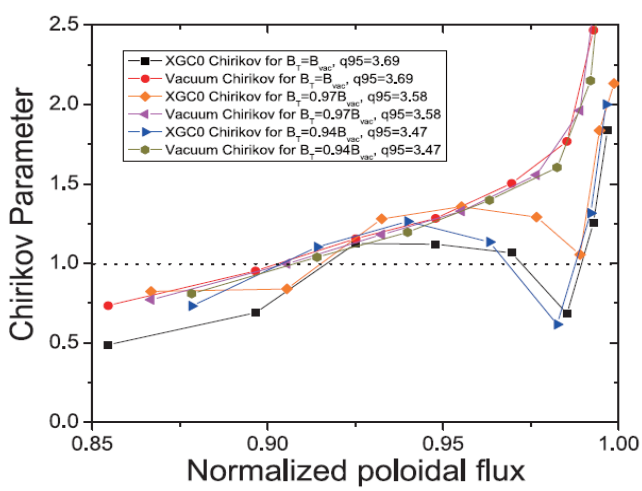


***Figure 9*** *Radial distribution of Chirikov parameter for three different $q_{95}$ values: $q_{95}$=3.58 inside the suppression window, and 3.47 and 3.69 outside it.*

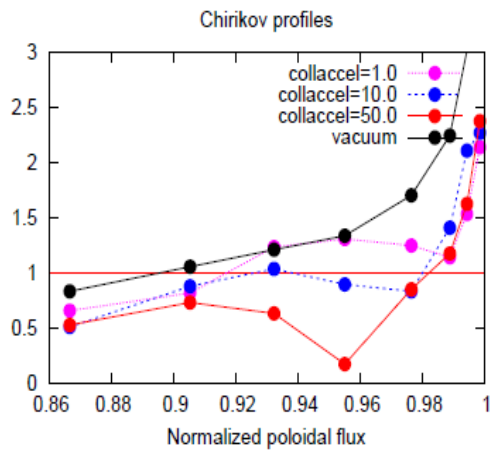


***Figure 10*** *Dependence of the Chirikov parameter profile on the electron collisionality. A sharp decrease in the stochastic connection between pedestal top and divertor plate can be seen as the collisionality increases by factor of 10.*

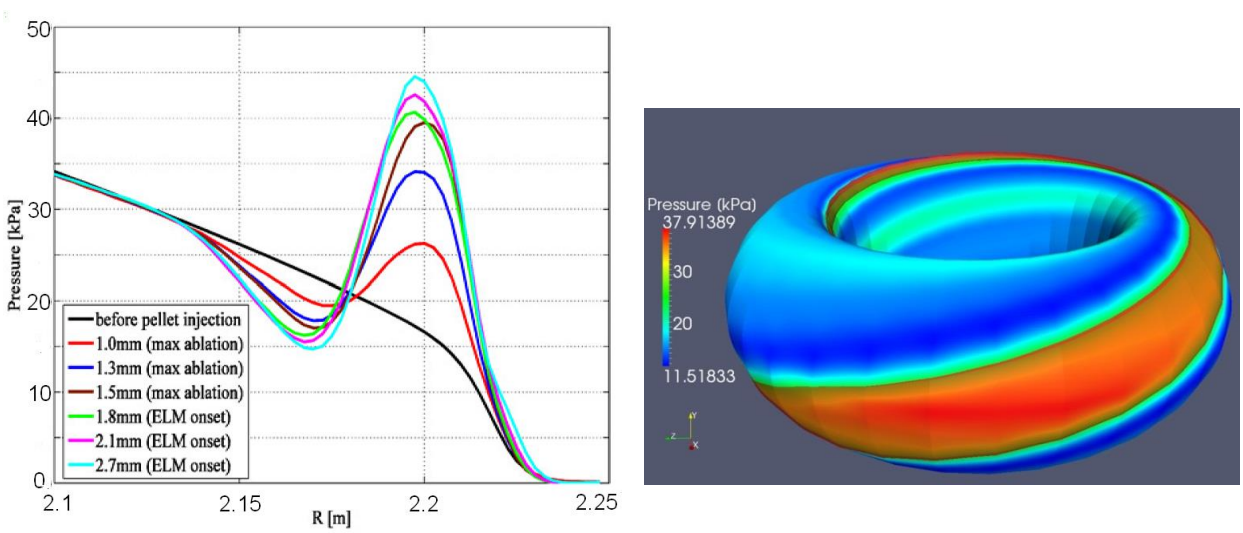


***Figure 11*** *(left) The simulated perturbed pressure profile in the mid-plane of a DIII-D plasma for various pellet sizes, at the time of the MHD onset or at the time of maximum ablation rate. (right) The 3D structure of the field aligned pressure perturbation for a 1.3mm pellet.*